STARS

Electronic Theses and Dissertations, 2004-2019

2013

Generation And Printing Of Strictly Monodisperse Droplets

Hongxu Duan

University of Central Florida

Part of the Mechanical Engineering Commons

Find similar works at: https://stars.library.ucf.edu/etd

University of Central Florida Libraries http://library.ucf.edu

GENERATION AND PRINTING OF STRICTLY MONODISPERSE DROPLETS

by

HONGXU DUAN
B.S. University of Agriculture of China, 2005

A thesis submitted in partial fulfillment of the requirements
for the degree of Master of Science in Mechanical Engineering
in the Department of Mechanical and Aerospace Engineering
in the College of Engineering and Computer Science
at the University of Central Florida
Orlando, Florida

Spring Term
2013

ABSTRACT

Highly monodisperse droplets are attracting great attention both in many research areas, such as aerosol science, combustion, and Nano-manufacturing. This thesis invents a novel aerosol generator: "Periodic Electro Hydro-dynamic Chopper" termed as "PEHD chopper", and develops a new method to directly print micro-patterns with monodisperse droplets. The principle of the PEHD chopper is to use the fringe electric field of a capacitor to introduce controlled perturbation on a liquid jet.

We first derived the governing equations for a circular inviscid liquid jet under transverse electric fields. The electric fields were obtained through numerical simulation. Then we used a high speed camera (up to one million frames per second) to visualize the jet break-up as well as the droplets' size and shape.

The experiments show that the PEHD chopper can effectively "chop" a neutral micro-jet and generate highly monodisperse micro-droplets, which diameter range from 100 μm to 500 μm. To reduce the droplet size, PEHD chopper with a butterfly design is applied on a typical single electrospray. In this configuration, the jet swings at long wavelengths ($\lambda > \lambda_R$), where λ_R is the Rayleigh wave length, but breaks up into highly monodisperse droplets near $2\lambda_R$ and λ_R without satellite droplets. The butterfly configuration combined with electrified jet expands the diameter range into 20 μm to 100 μm.

Finally, we demonstrate the electrospray printing of Polymer Derived Ceramics (PDC) for sensor applications in harsh environment. A modified single ES with an additional driving electric field is used to directly print PDC precursor without mask, we achieved 1D feature as narrow as 35 µm and a micro pentagram pattern. Moreover, after pyrolysis of PDC at 1100 °C in nitrogen, amorphous alloys of silicon, carbon and nitrogen (SiCN) are obtained. The samples exhibit excellent good integrity and adhesion to the substrate.

ACKNOWLEDGMENTS

First of all, I thank all the thesis committee members for their great help, instruction and service. Especially, I want to thank my advisor Dr. Weiwei Deng, who was encouraging and supporting me all the way along my graduate study. From him I learned not only research skills, but also the good characteristics and principles of being an engineer, such as being logical, creative, responsible, careful and persist. All these will be very helpful in my future career.

Secondly I want to thank all my lab mates for their tremendous help. We really make steady progress and have a great time together on research.

Thirdly, I want to thank my parents, who gave their best to raise me up unconditionally and provide me a good environment. I am grateful for their strong backup, respect and suggestions whenever I make my decisions. I am fortunate enough to own such lovely parents with beautiful minds.

Lastly, I want to thank my wife Dr. Cheng Li who is always accompanying and supporting me. We are always heading towards the happier and healthier life. Only God knows how much I love you and our coming son. Hope Jesus Christ blesses our family.

TABLE OF CONTENTS

LIST OF FIGURES

LIST OF TABLES

CHAPTER 1 INTRODUCTION

1.1 Motivation: the need for strictly monodisperse droplets

The jets and the droplets breaking up from jets are ubiquitous in our daily life. The most common example should be water coming from a faucet. In Figure 1.a, the tap water cannot break up into droplets before it hits the sink due to the large jet diameter, the high initial velocity, and the short residence time (Eggers and Villermaux, 2008). Closing the valve gradually, the jet length is reduced (Figure 1.b and Figure 1.c) and droplets are formed from jet breakup. Finally, when the flow rate is reduced more, only dripping can be observed (Figure 1.d.).

a   b   c   d

Figure 1: Flow of tap water through a faucet at decreasing flow rates

In light of the behavior of jets, people utilize jets and droplets for cleaning, painting and agricultural irrigation by changing the nozzle diameter and pressure. When water jets reach a higher speed, they can be used for cutting tissues, meat and even metal plates shown in Figure 2 (Eggers and Villermaux, 2008).

Figure 2: A high pressure jet is cutting aluminum sheet (Eggers and Villermaux, 2008)

To generate droplets, there are numerous commercialized atomizers which are categorized by different driving mechanisms, such as pneumatic, hydraulic, ultrasonic and electrostatic. For example Figure 3 depicts the principle of an ultrasonic atomizer. The authors used several interfacial wave patterns in a forced sessile drop as the forcing amplitude (B. Vukasinovic, M. K. Smith and A. Glezer, 2007).
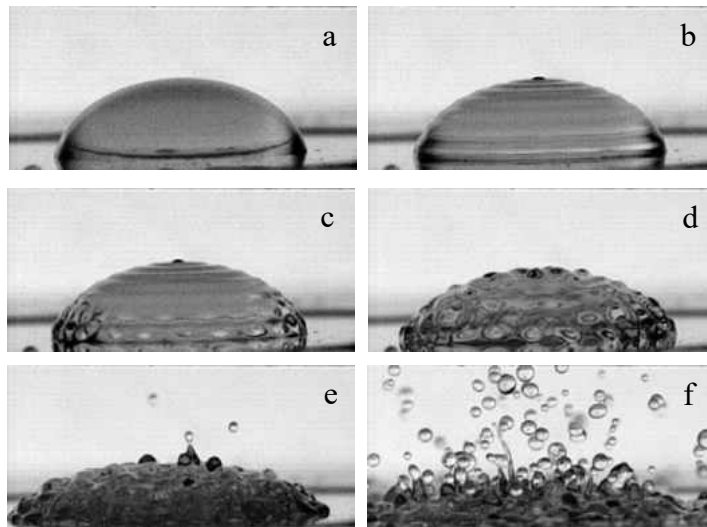
Figure 3: The development of droplets driven by ultrasonic method. (*a*) unforced (*b*) axisymmetric waves (*c*) coupling of axisymmetric and azimuthal waves (*d*) pre-ejection state (*e*) ejection onset (*f*) atomization (B. Vukasinovic, M. K. Smith and A. Glezer, 2007)

Another example of an atomizer is electrostatic spray implemented in auto body painting. Because of the attractive force between charged painting particles and painting objects, the electrostatic spray can lead to higher efficiency and more even coatings for auto bodies in a low pressure setting. The printing pattern and thickness can be well controlled by various types of orifices and hot spray.

It is important to notice that the process which unites these examples is jet breaks up into droplets. The jet breakup is a fascinating subject of extensive study (S. Chandrasekhar, 1981) because of both the theoretical value and widespread applications (S. P. Lin and R. D. Reitz, 1998). Micron level monodisperse droplets, or droplets with narrow (<1%) size distributions, have recently gained more and more attention. Monodisperse droplets are favored by such applications as ink jet printers, which require the prompt and precise formation of an ink drop at certain points (I. Rezanka and J. M. Crowley, 1986). Another instance is in biological and medical study, where monodisperse droplets carrying individual cells can be classified and deflected to the desired destination (Hrdina, D. W. and Crowley, J. M, 1989). Highly monodisperse droplets also find applications in other areas like photonic crystals, lasing in whispering gallery mode (Figure. 4), combustion, additive manufacturing and aerosol instrument calibration.
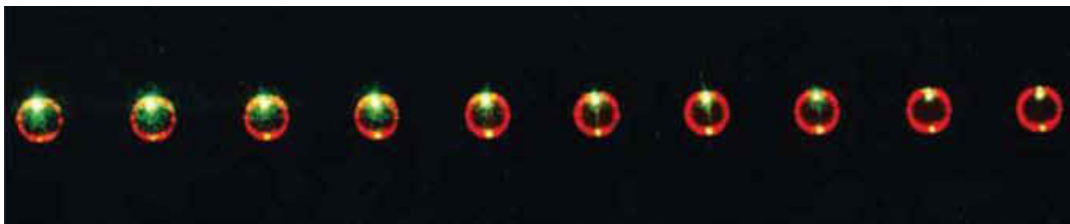
Figure 4: Laser emission from the droplet stream within the first few millimeters of the vibrating orifice (Richard K. Chang et al, 1986)

Therefore this thesis is motivated by the need to develop a new approach on the generation of micron level highly monodisperse droplets with zero satellite droplets.

1.2 The Rayleigh instability of liquid jets

The jet break up into droplets is a process governed by the instability of liquid jets. Laplace and Young first realized the surface tension as the source of instability in 1805. Namely, the role of surface tension is to minimize surface area, hence the jet radius becomes infinitesimal and finally breaks up (Eggers, 1997). In 1833, Savart performed a series of experiments relating droplet formation and the decay of jets. He showed that a tiny perturbation applied to the jet at the opening of the nozzle is accumulated into the instability of the jet and the jet will breakup when the instability reaches the radius of the jet. Mathematically, he noticed that the applied resonance frequency of the system is inversely proportional to the nozzle radius and proportional to the jet velocity (Eggers and Villermaux, 2008). Based on Savart's results and theories, Plateau pointed out that jet will become unstable to any perturbation which wavelength is long enough to reduce the surface area. However, the criteria for the exact wave length are not correct.

Rayleigh used linear perturbation theory and confirmed Savart's results and discovered that a liquid jet is intrinsically unstable to external perturbations with wavelength longer than the circumference of the jet. In addition, the instability grows exponentially and often the fastest growing wavelength λr_0 (about 9 times of jet radius) dominates the distribution of the droplet diameter, which is about 1.89 times of jet diameter.

Figure 5 shows typical pictures of a decaying jet of water under three different wavelengths (Rutland and Jameson, 1971). The bottom picture of Figure 5 is closest to Rayleigh mode with the most instability. Hence, by turning the wavelength λ to $9.19r_0$, the jet breaks up

regularly and breakup length is the shortest. By comparison, the longest wavelength 83.7 times of jet radius in the top picture of Figure 5 makes the phenomenon quite elusive. Rayleigh explained this as the harmonics inconvenience by using a musical instrument analogy.
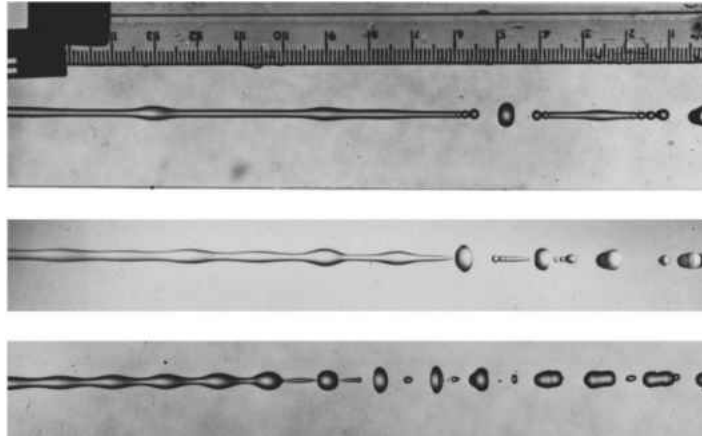
Figure 5: Photographs of a decaying jet (Rutland and Jameson, 1971) for three different frequencies of excitation

We can extend Rayleigh linear perturbation theory to control jet break-up and generate monodisperse droplets. In the next sub-section, we will review the existing experimental work on forced jets in accordance with monodisperse droplets generators.

1.3 Methods of introducing prescribed perturbations

1.3.1 Acoustic (loudspeaker)

In the 20th century, the acoustic stimulation on forced jets was a popular approach to generate definite perturbation that allowed experimentalists to study the physics of jet breakup. A typical apparatus by R. J. Donnelly and W. Glaberson (1966) is shown in Figure 6. With this

setup, the authors generated a vertical with jet diameter of 0.635cm to study the dispersion curve for induced disturbances on the jet.
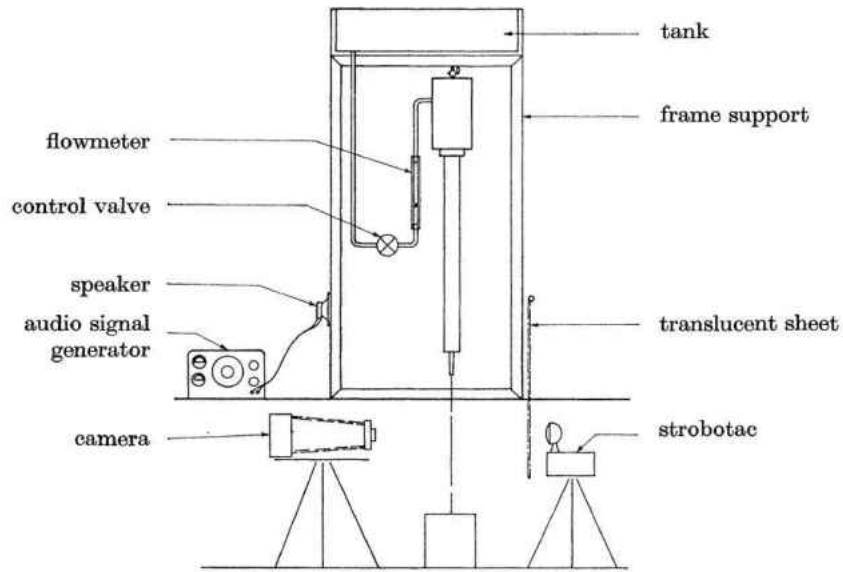
Figure 6: Sketch of the apparatus showing the principal parts of the experimental arrangement (R. J. Donnelly and W. Glaberson, 1965)

Structurally, the nozzle with the tank was mounted on a large steel frame which sits on rubbers. The loudspeaker that was driven by an audio oscillator was clamped to the frame to introduce high perturbation amplitude. To get higher perturbation, a long pin coupling to the center of the speaker was required to directly contact the jet itself.

1.3.2 Mechanical (vibrating orifice)

Another common excitation source for introducing the perturbation is piezoelectric actuator which is connected in the liquid line. Under alternating driving signals, the piezoelectric actuator superimposes a periodic vibration on the back pressure which drives the jet.

Such a vibrating orifice aerosol generator (R. N. Berglund and B. Y. H. Liu, 1973) has been commercialized (TSI model 3450) and used as sizing standard and lasing droplets because

of the strictly monodisperse droplets generated. The mechanism and assembly of droplet generation are shown in Figure 7. Depending on different orifice sizes, the orifice can generate highly monodisperse droplets (typical geometry relative standard deviation less than 1.01%) with diameter ranging from 20μm to 400μm. For instance, with a 10μm orifice, TSI 3450 can generate droplets of about 20μm diameter.
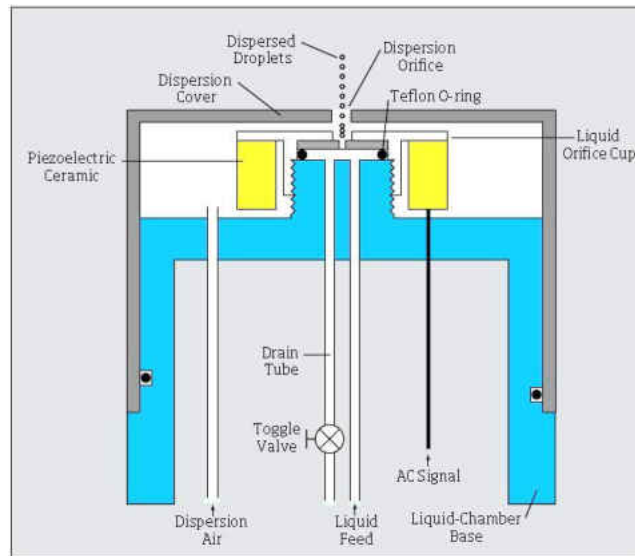
Figure 7: Mechanism of droplet generation and dispersion assembly (TSI model 3450)

1.3.3 Electro-hydrodynamic (electrode with circular hole)

Compared to the previous methods we have discussed, a less common approach for introducing perturbation is to use electric fields. The electric field can be AC, or AC superimposed on a DC field which accelerates the liquid jet. This intermittent stimulation approach is termed as electro-hydrodynamic excitation (Hrdina and Crowley, 1989) and abbreviated as "EHD excitation".

EHD stimulation was first proposed and employed by Goedde and Yuen (1970) for jet with 1~2 mm diameter. The experiment arrangement is shown in Figure 8. They applied a high

voltage electrical AC signal between the jet and the brass plate. The plate with a hole in the center for the jet passing through was placed about 1/8 in. below the nozzle orifice. In this fashion, the resulting axisymmetric electrical force will deform the surface of the jet and lead to break up of the jet.
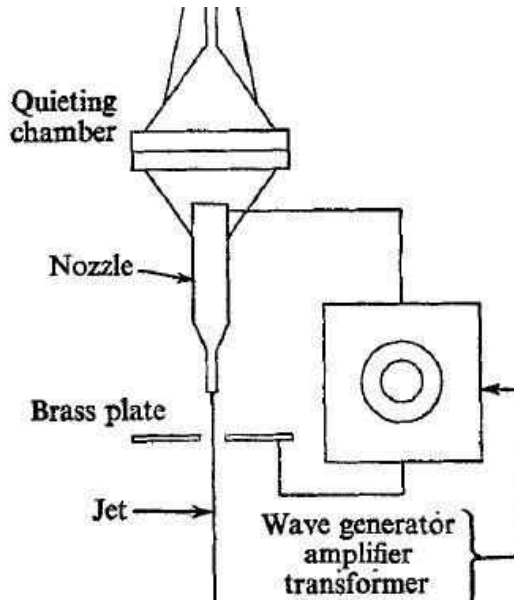
Figure 8: Sketch of the apparatus showing principal parts of the experimental arrangement (Goedde and Yuen, 1970)

The essences of EHD stimulation have been characterized by Joseph M. Crowley (1982). He pointed out that the electric field with proper frequency will induce the compression and expansion on the jet, which will later break up the jet into droplets. Importantly, Crowley mathematically analyzed the electric pressure inside the jet by setting up a model with a cylindrical liquid jet entering a circular electrode. Figure 9 shows the parameters and schematic of the model. The pressure component at the frequency ω is written as Equation (1.1):

$$p_0 = -\frac{\varepsilon V_{eff}^2}{2a^2 \ln^2(b/a)},\tag{1.1}$$

where the effective voltage at ω is Equation (1.2):

$$V_{eff} = (2V_{dc}V_{ac})^{1/2}. \qquad (1.2)$$

These two equations indicate that the breakup length is only dependent on the electrode dimensions jet radius "a" and inner radius of the circular electrode "b", applied voltage, and the permittivity of material "ε". In addition, Crowley explained the critical component from the EHD perturbation should be the transverse velocity excited on the jet, because the growth over one wavelength (U_0/ω) is relatively small.
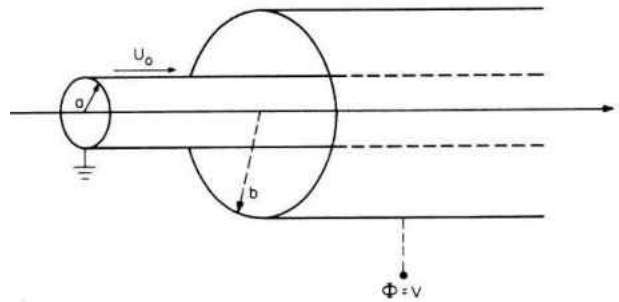
Figure 9: A liquid jet entering an electrode (Joseph M. Crowley, 1983)

H. Gonzalez and F. J. Garcia (2009) also modified the design of EHD stimulation by replacing the common electrode with an iris diaphragm and added a second shielding diaphragm located a few millimeters below the first stimulation electrode. The detail of the stimulation and shielding electrodes are shown in Figure 10. The function of the shielding electrode is to protect most of the jet from the electric field excitation. Consequently, this becomes worthwhile for very precise measurement of the growth rate of instability.
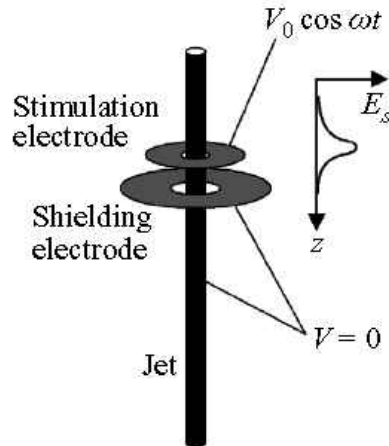
Figure 10: Detail of the stimulation and shielding electrodes (H. Gonzalez and F. J. Garcia, 2009)

1.3.4 Discussion of previous work

From the review of main means of introducing perturbation on forced jets, EHD is the most promising approach since it can promptly, precisely and conveniently control the excitation amplitude and wavelength which is prescribed by signal generator (H. Gonzalez and F. J. Garcia 2009). Another advantage of EHD stimulation is the flexibility of relative position between the jet and the stimulator due to its direct effect on jet surface without contact. This might contribute to an ink jet printer with longer break off distance which wins more space for the nozzle design (Rezanka, 1986). While the EHD stimulation usually generates weaker perturbation than the acoustic loudspeaker does, however, with the help of transformer or amplifier, this issue can be solved by proper design of electrode and use of amplifier.

Another common disadvantage shared by all the methods above is that the droplet size is highly dependent on the orifice diameter. Rayleigh's theory suggests that the generation of smaller droplets requires jet diameter reduction. However, forming jets by forcing liquid through an orifice, although convenient, is extremely challenging for orifice diameter below 10 μm, due to the profound viscous effect at small scales. For a certain flow rate, the pressure gradient scales

10

with d_o^{-4}, where d_o is the orifice diameter. To solve this problem, we notice that an electrified jet formed from the Taylor cone (Taylor, 1964) has virtually no limit on how small the jet diameter could be, because the jet forms at the liquid-air free surface, eliminating the liquid-solid interface and associated viscous effect imposed by no-slip conditions. Indeed, the electrospray (formed by natural breakup of electrified jet from the Taylor cone) is the dominant method of generating quasi-monodisperse droplets for diameter from 10s of micrometers to a few nanometers. For this reason, this thesis will also study how to apply EHD stimulation to electrified micro jets generated from Taylor cones.

1.4 Thesis organization

This thesis is organized as follows:

Chapter one introduces the motivation and background of the monodisperse droplets and reviews previous work on generating monodisperse droplets. These give us a starting point and help us better understand the theory of this realm.

Chapter two describes a non-intrusive approach to generate periodic electro hydrodynamic perturbation. With this approach, we can generate highly monodisperse droplets with diameter from 100μm to 500μm. We studied the electric field of PEHD chopper using both by numerical simulation and analytical model.

In chapter three, we change PEHD chopper into a symmetrical butterfly structure and it enables the device to generate micro-droplets from 20μm to 100μm. We find that the jet swings at long driving signal wavelengths ($\lambda \gg \lambda_R$), but breaks up into highly monodisperse droplets near $2\lambda_R$ and λ_R without satellite droplets.

In chapter four, we develop a novel approach to directly print polymer derived ceramics (PDC) with a modified electrospray. We demonstrated the good integrity and surface quality of printed pattern after pyrolysis of the PDC samples.

Chapter five summarizes our conclusions and recommends potential that are worthwhile of future investigations.

CHAPTER 2 PERTURBATION OF NEUTRAL MICRO-JETS USING CAPACITOR-TYPE CHOPPER

2.1 Momentum equation of the neutral micro-jet

We first set up a model to analyze the perturbation response to the electrical and geometrical parameters of the chopper. Following Canan-Calvo (A. M. Gañán-Calvo, 1998), we can re-write the momentum equation for a slender jet under electric field as:

$$\frac{d}{dz}[P_g + \frac{\gamma}{\xi} - \frac{1}{2}\varepsilon_0 E^2 + \frac{\rho_l Q^2}{2\pi^2 \xi^4}] = 0, \tag{2.1}$$

where P_g is the atmosphere pressure, ρ_l is the liquid mass density, and Q is the liquid volumetric flow rate. In Equation (2.1), the combination of the first three terms is the total pressure inside the liquid jet. Further, inexplicit in Equation (2.1) is that both internal viscous loss and the shear stress at the liquid-air interface are neglected.

Since $Q = \pi \xi^2 v_j$, and use $\beta^2 = \rho \xi v_j^2 / \gamma$, we can rewrite Equation (2.1) as:

$$\tilde{\xi} = \frac{d\xi}{\xi} = -\frac{\varepsilon_0 E \cdot (\partial E / \partial z)}{(2\beta^2 + 1)\gamma / \xi} dz. \tag{2.2}$$

Where β is defined as Webber number. Equation (2.2) suggests that the perturbation not only scales with the magnitude of the fringe field, but also scales with the gradient along z-direction of the fringe field. We can understand the gradient of the fringe field as an indicator of the "sharpness" of the chopper.

2.2 Fringe electric fields of a capacitor

To solve Equation (2.1), we first need to quantify the electric field E. The fringing electric field at the edge of capacitor has significant horizontal component E_x, as shown in Figure 11. E_x induces charge on the jet surface and generates an attracting force between the jet and the capacitor. The AC voltage causes periodic changes in the fringe electric field, and the Electro-hydrodynamics (EHD) perturbation force is expected to perturb the jet and "chop" it. The jet subject to the EHD perturbation will breakup orderly and generate droplets with high degree of monodispersity.
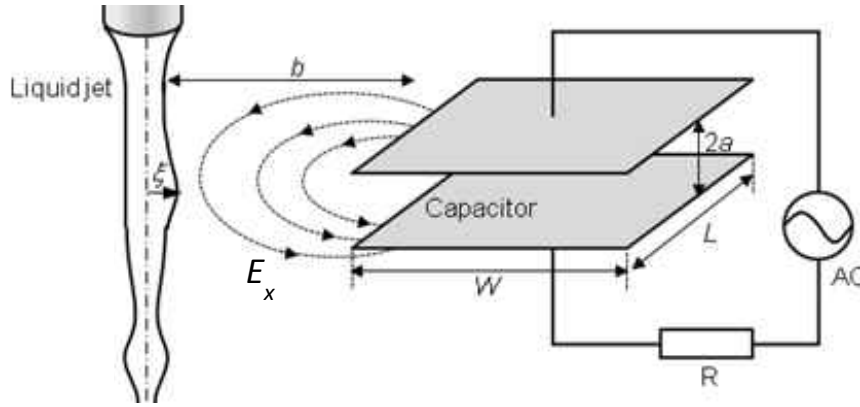
Figure 11: Schematic of capacitor EHD chopper

2.2.1 Analytical solution of the fringe electric fields

Next we consider the fringe electric field that is norm to the jet surface. The approximate solution of the fringe electric field above the top capacitor electrode (or below the bottom electrode) has been determined by Parker (2002):

$$E = \frac{Vz}{2\pi(z^2 + b^2)},$$ (2.3)

where V is the voltage applied to the chopper/capacitor, b is the distance between the jet and the edge of the capacitor; z is the vertical distance from the jet surface to the upper capacitor. The solution is based on the approximation that $2a << W << L$, where 2a is the separation between the two electrodes of the capacitor, W is the width of the capacitor and L is the length of the capacitor. Equations (2.2) and (2.3) yield:

$$\tilde{\xi} \propto \frac{V^2 z(b^2 - z^2)}{(z^2 + b^2)^3} . \qquad (2.4)$$

Expression (2.4) suggests that initial perturbation is indeed proportional to $V_{p\text{-}p}^2$. This is expected because both the electric field and gradient of electric field scale with $V_{p\text{-}p}$. The square of the AC voltage doubles the driving signal frequency to $2f$, and yields the wave length of perturbation as $\lambda = v_j/2f$, with f being the applied signal frequency.

2.2.2 Numerical simulation of the electric field

To better understand our cases, we use a Commercial Finite Element Analysis Software Package (COMOSOL 4.2) to numerically simulate the E_x along the jet surface.

We set typical experiment parameters in the model as follows: applied AC amplitude, V_{p-p}=300V, jet radius, ξ=75μm, capacitor thickness t=100μm, distance between two blades, $2a$=300μm. Keeping the other parameters same, we run each case by decreasing the gap between the edges of capacitor and jet surface (b) from 500μm to 100μm at 100μm intervals. Figure 12 shows the simulation result of electrical field change in PEHD chopper experiment.
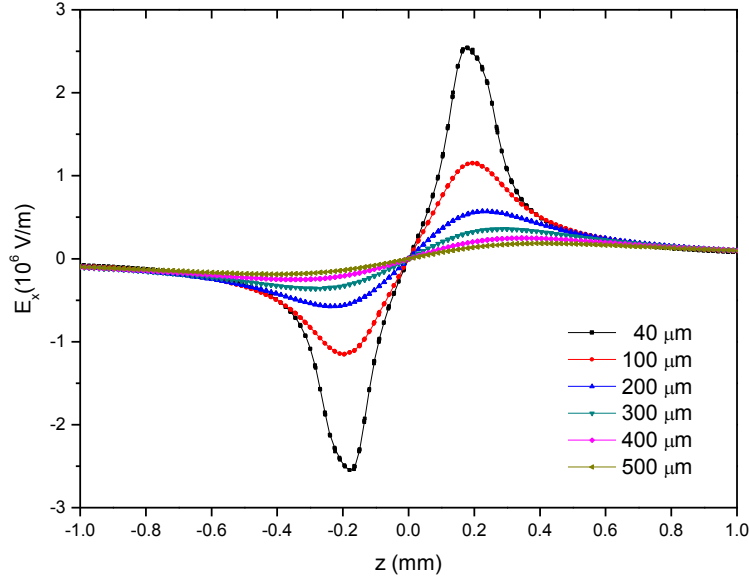
Figure 12: Numerical simulation of the X component of the fringing electric field of PEHD chopper

2.2.3 Discussion of the range and magnitude of the field

To set the differentiation $d\xi/dz$ equal to zero in Equation (2.4), it is worth noticing that the maximum perturbation is reached at z/b=0.36 for any given b. At this ratio, the dimensionless perturbation scales with b^{-3}, indicating that the effectiveness of the capacitor increases rapidly as b decreases. The ratio also suggests that as b approaches zero, the maximum perturbation appears at z~0, or very close to the edge of blade electrode.

To provide a more meaningful comparison, we change y axis into x_0*E_x and x axis into z/x_0 in Figure 13. The term z/x_0 compares the relative distance from the edge of the chopper to jet surface. Figure 13 suggests that when plotted using x_0*E_x and dimensionless distance, the electric fields are self-similar: x_0*E_x is comparable to V_{p-p} and the peak electric field is located at $z/x_0 \sim 1$.

16
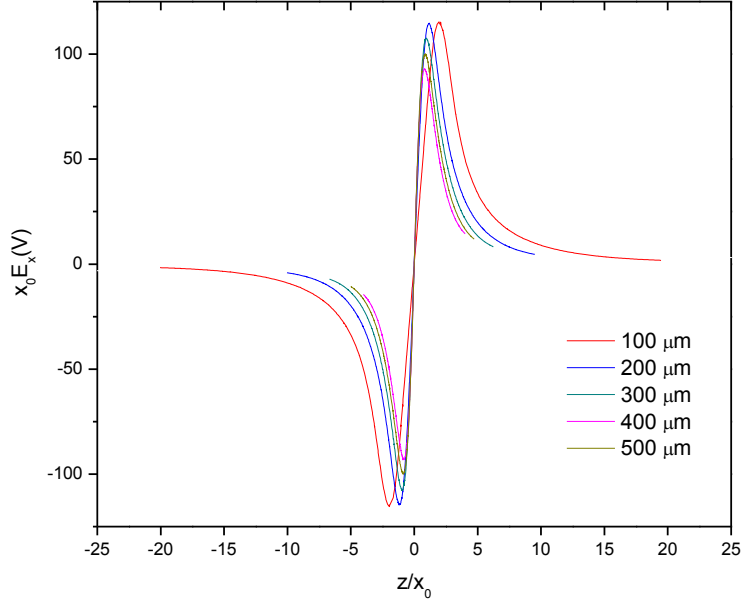
Figure 13: Numerical electrical fields' simulation with modified ordinates

2.3 Experimental setup and results

2.3.1 Overview of setup

Figure 14 depicts the experimental setup. The ethanol micro jet (radius $r_0=75\mu m$) is generated by forcing ethanol (200 proof) out of a 30 gauge stainless steel needle (inner diameter 159 μm) using a high pressure syringe pump at flow rate of 100 to 200 mL/h. The jet Weber number is defined as $\beta^2=\rho r v_j^2/\gamma$, where ρ is the liquid mass density, r is the jet radius, v_j is the jet velocity, and γ is the liquid interfacial tension, respectively (Eggers, 1997). For a typical flow rate of 100 mL/h in this work, the Weber number β^2 is of order 10. The Reynolds number of the jet is about 100.

The transverse perturbation is introduced by the fringe electric field of a specially designed capacitor (chopper). Both electrodes of the capacitor are sharp razor blades, separated

17

by a Kapton tape spacer, forming a gap (2a) of 400 μm. Electrically, the chopper is connected to a sinusoidal alternating current (AC) signal source, with adjustable $V_{p\text{-}p}$ (peak-to-peak voltage) from 0 to 400V. Mechanically, the chopper is mounted on a linear translational stage to precisely control b (the distance between the edges of the capacitor to the jet surface). The phenomena are recorded with a high speed camera (Phantom v12.1) coupled with a microscope with 2× or 4× magnification. A collimated LED light source is placed behind the jet and pointing to the camera to form a shadowgraph configuration. The camera is operated at a speed of 22000 frames per second with a shutter time of 10 μs.
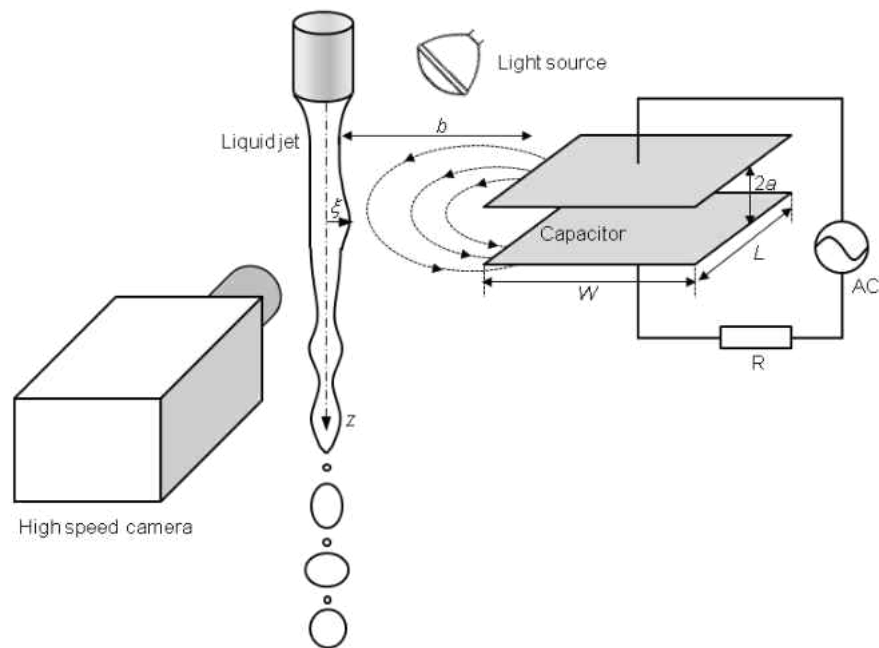
Figure 14: Experimental setup of the jet under transverse electro-hydrodynamic perturbation

18

2.3.2 Perturbation versus gap

Figure 15 shows the response of the liquid jet to the perturbation as the chopper approaches the jet. The edge of the chopper is perpendicular to the jet as well as the image plane. The driving voltage $V_{p\text{-}p}$ and frequency are 300V and 1.15 kHz respectively. The jet is affected by the perturbation for all cases, with increasing initial perturbation $\Delta\xi$ as b is reduced.
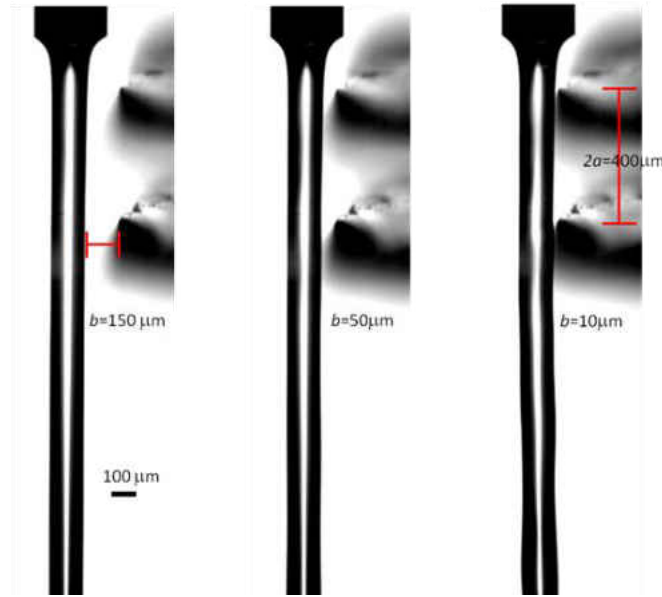
Figure 15: Visualization of jet under transverse electro-hydrodynamic perturbation

2.3.3 Growth rate versus voltage

For practical applications, it is usually not feasible to place the chopper very close to the jet, say b<50 µm, and consequently the initial perturbation $\Delta\xi$ is difficult to measure directly from the image. However, $\Delta\xi$ can be derived from the jet breakup length. For an axial symmetric slender jet, we denote jet surface profile as $\xi(z)$, where z is the distance from the exit of the nozzle, and ξ is the jet radius at location z. The dimensionless growth of perturbation is

$$\widetilde{\xi} = \Delta\xi / r_0 = \widetilde{\xi}_0 \exp(\overline{\omega}\omega_0 t). \tag{2.5}$$

Here $\widetilde{\xi}_0$ is the initial dimensionless perturbation $\overline{\omega} = \omega / \omega_0$ is the dimensionless growth rate, and ω_0 is defined as:

$$\omega_0 = \sqrt{\gamma / (\rho r_0^3)}. \tag{2.6}$$

With the parameter used in this experiment, ω_0=8145 Hz. Rayleigh's linear perturbation theory shows that the growth rate is a function of reduced wave number $x=2\pi r_0/\lambda$, where λ is the wavelength of the periodic perturbing force, $\lambda=V_j/2f$, with f being the applied signal frequency. For inviscid jet, the Rayleigh solution states:

$$\overline{\omega}^2 = \frac{xI_1(x)}{I_0(x)}(1-x^2), \tag{2.7}$$

where $I_0(x)$ and $I_1(x)$ are the Bessel functions of zero and first order. Equation (2.7) is plotted in solid curve in Figure 17. The jet is unstable for any perturbations with $x<1$; the fastest growth rate is ω/ω_0=0.366 when x_R=0.697, or the Rayleigh mode. When the driving frequency is close to 50% of the Rayleigh frequency, the perturbation grows faster, and the jet breaks up earlier. Figure 16 shows the breakup length L (the distance between the point of perturbation and the location where ξ becomes zero) can be reduced by ~3mm, or 20 folds of the jet diameter at ~50% of the Rayleigh frequency (approximately 1.1kHz). At the shortest breakup length, or maximum growth rate of the initial perturbation, we measured the diameter of the droplets downstream through edge detection of hundreds of frames from the high speed video footage. The result shows the droplets are highly monodisperse, with relative standard deviation of the diameter less than 1%.
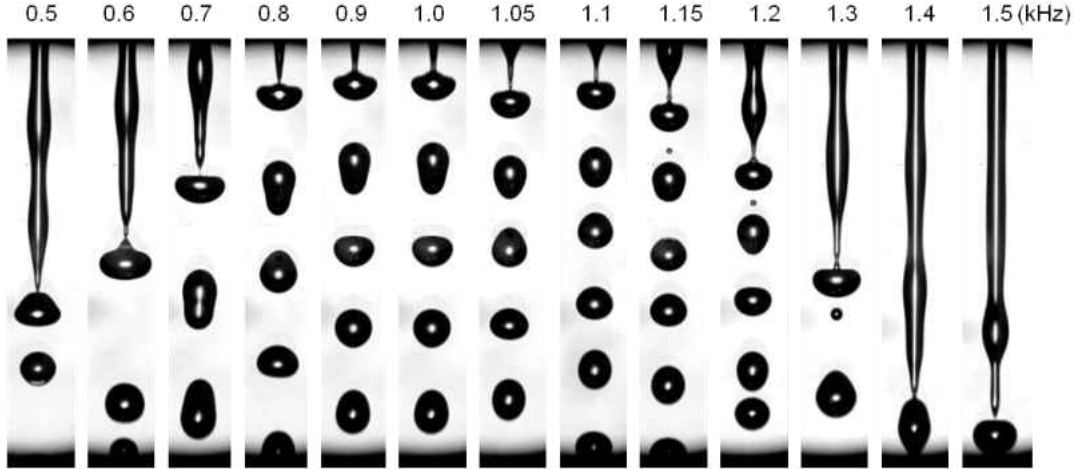
Figure 16: The breakup length at different driving frequencies. The gap b is 400 μm. V_{p-p}=330V

Equation (2.5) suggests that from breakup time, one can get the dimensionless growth rate. The breakup time t can be experimentally determined through measuring the breakup length: $t= L/v_j$. We have varied the driving frequency, thus changing the wavelength as well as the reduced wave number x_R. We plot the experimental results (red square) together with the classic Rayleigh solution (solid black curve) in Figure 17. Although the general trend of the experimental data is in agreement with the Rayleigh solution, the discrepancy becomes obvious as the reduced wave number moves away from x_R. This may be due to more complicated higher harmonic perturbations, as well as the intrinsic difficulties in obtaining accurate measurements in growth rate (Eggers, 1997). In addition, the micro jets studied in this work are substantially smaller than the jets in frequently cited literature: r_0>499μm in Donnelly and Glaberson and Goedde and Yuen, therefore higher measurement uncertainties can arise because of smaller jet diameters. Also, the Reynolds number in this work is of order 100, which makes the inviscid assumption not as good as larger jets.
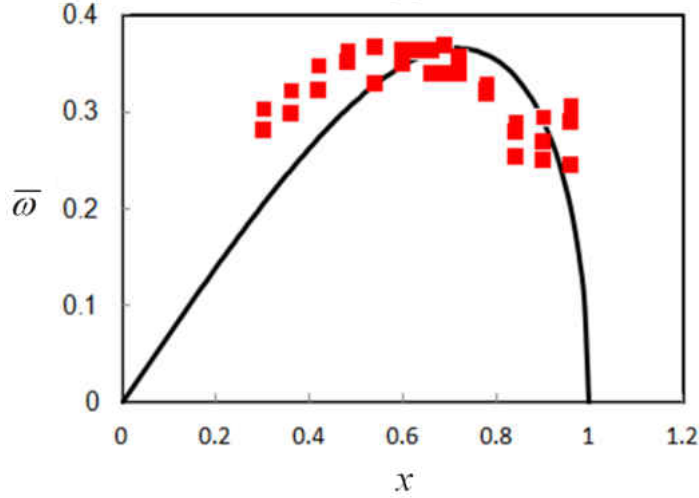
Figure 17: Growth rate vs reduced wave number

The force that causes the perturbation is the norm component of the Maxwell stress at the liquid/gas interface, $\tau_e = \varepsilon_0 E^2/2$, where ε_0 is the permittivity of the vacuum, and E is the norm electric field at the interface. The latter is related to the surface free charge density σ_e through $E = \sigma_e/\varepsilon_0$. Although the process is dynamic and transient, the ethanol jet can be considered as equal-potential because the liquid charge relaxation time (J. R. Melcher and G. I. Taylor, 1969) ($t_e = \varepsilon/K \sim 1$ µs) is much shorter than the period of driving AC signal (about 1ms), where $K = 10^{-4}$ S/m is the electric conductivity of the ethanol used in this work. In other words, during each AC signal cycle, the free surface charge has enough time to redistribute and make the jet surface reach the same electric potential.
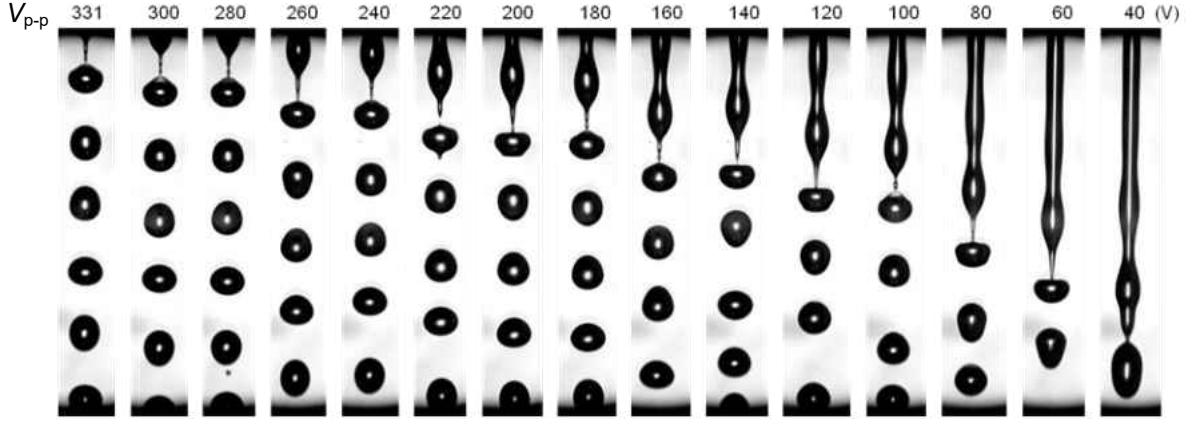
Figure 18: Jet breakup locations as a function of V_{p-p} at fixed frequency. Jet radius is 75 μm

Figure 18 shows the location of jet breakup as a function of V_{p-p}. The reduced wave number is chosen as x_R for fastest growth. As the voltage increases, the jet breaks up earlier, indicating stronger perturbation is induced at higher V_{p-p}.

Since the growth rate is known at Rayleigh mode ($\omega//\omega_0$=0.366), Equation (2.5) allows us to calculate the initial perturbation $\Delta\xi_0$ from breakup length L. We plot $\Delta\xi_0$ against V_{p-p}^2 in Figure 19. First we note that for Rayleigh instability to develop and generate monodisperse droplets, the initial perturbation is from 4 nm (V_{p-p}=40V) to 80 nm (V_{p-p}=330V). To put this value into context, typical natural initial perturbations is $\Delta\xi_0/r_0 \sim e^{-12} \sim 10^{-5}$, or $\Delta\xi_0 \sim 1$ nm. Secondly, the initial perturbation $\Delta\xi_0$ appears to be linearly proportional to V_{p-p}^2.
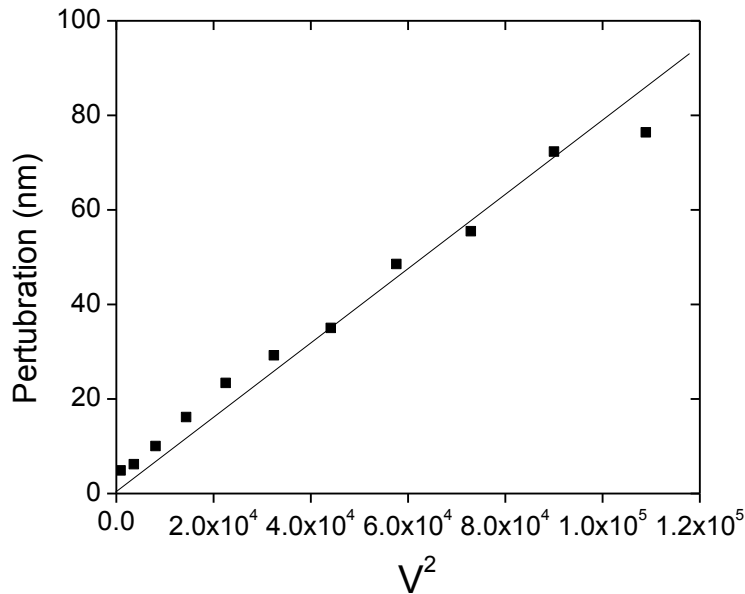
Figure 19: The linear relationship between the magnitude of perturbation (calculated from Equation (2.5)) and the V_{p-p}^2 of the driving signal.

2.4 Scale-up of the perturbation

Since the fringe field of the chopper is essentially two dimensional, the same chopper can be applied to multiple jets. We machined a four-nozzle linear array using a precision drilling and milling process out of aluminum (Lojewski et al, 2012) (Figure 20.a). The nozzles have equal spacing of 500 μm and produce four nearly identical jets (Figure 20.b). The chopper is placed near the exit of nozzles, with the chopper plane perpendicular to the linear array and the edge parallel to the jet array. Figure 20.c shows that all four jets break up earlier under the periodic perturbation from the chopper. This demonstrates that the PEHD chopper is a scalable device that can operate on multiple jets for generating strictly monodisperse micro droplets at high throughput.
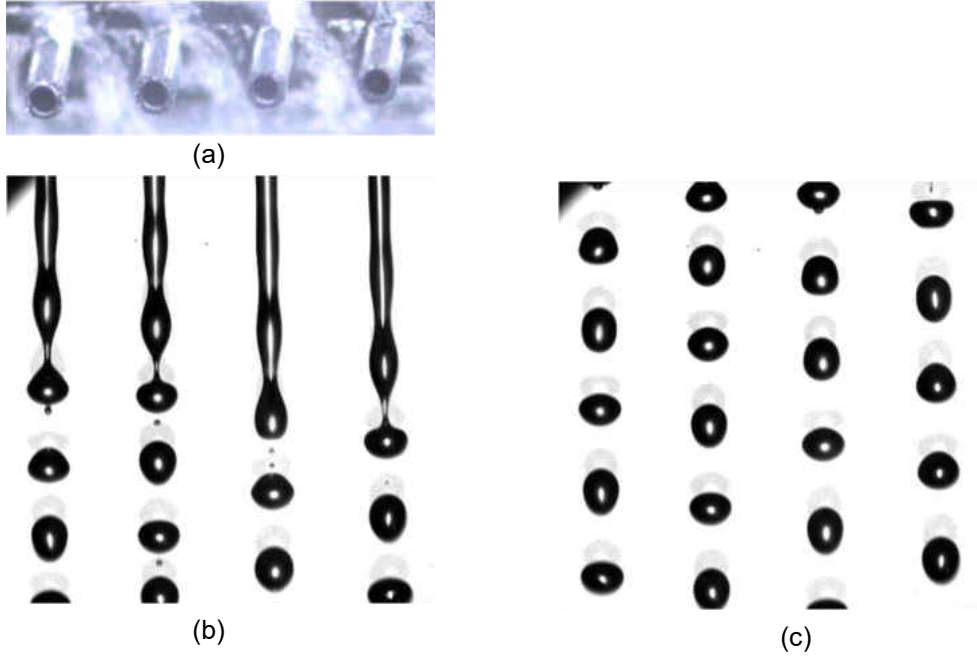
Figure 20: Multiple jets that experience transverse perturbation by the same capacitor. (a) The manifold of four nozzles (nozzle spacing: 500 μm; nozzle OD=200μm, ID=100μm); (b) the natural breakup of the four jets; (c) earlier breakup after the transverse perturbation is applied. Note the absence of satellite droplets in all four jet breakups.

CHAPTER 3 PERTURBATION OF ELECTRIFIED OF MICRO-JETS

3.1 Fringe electric fields of butterfly electrodes

3.1.1 Analytical solution

Due to the significance of the electric field, first we will find analytical and numerical solutions. Generally the "butterfly electrodes" chopper, consists of two sharp blades with edge face each other with separation *2a*. The two blades are connected to AC electrical field. Assume the two plates are semi-infinite, and then the problem becomes a two dimensional as shown in Figure 21. For any given moment, it can be treated as a steady state problem with the left edge at potential $-V_0$ and right edge at potential V_0. By symmetry the y plane has zero potential. Our goal is to solve the Laplace equation $\nabla^2\phi = 0$ with the specified boundary conditions as shown in Figure 21.
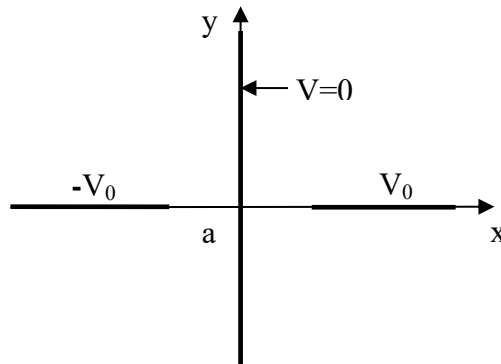
Figure 21: 2D problem of electric field

Using $x^* = x/a$, $y^* = y/a$ and $\phi^* = \phi/V_0$ to non-dimensionalize the problem, the Laplace equation (Zill and Wright, 2009) becomes $\nabla^2 \phi^* = 0$ with the boundary condition specified in Figure 22 (we only consider the right half plane since the problem is symmetric).
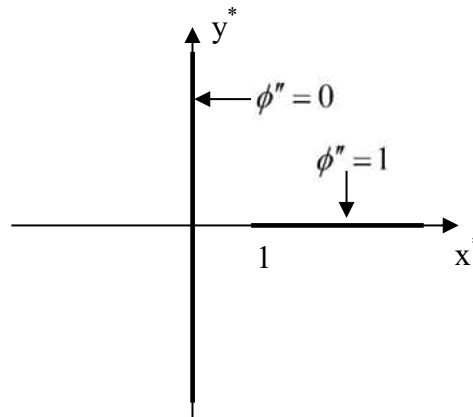
Figure 22: 2D problem of electric field after non-dimensionalizing

For simplicity we will omit the asterisk and consider the right half plane problem specified in Figure 22. The conformal mapping (Zill and Wright, 2009) $z = \sin w$ maps the strip $0 \leq \xi \leq \dfrac{\pi}{2}$ in the w plane to the right half plane (Figure 23), where $\xi = \dfrac{\pi}{2}$ is mapped to the boundary in the x axis $y = 0, x \geq 1$ and $\xi = 0$ is mapped to the y axis. This mapping and the mapping of the corresponding boundary condition are shown in Figure 23.
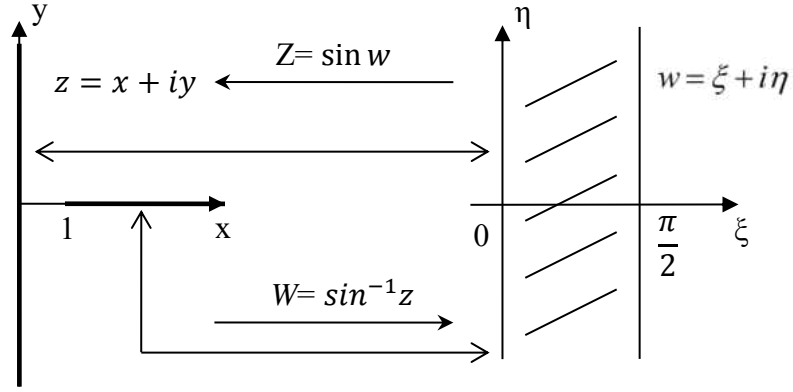
Figure 23: Conformal mapping (Zill and Wright, 2009) of z domain to w domain, where the geometry has been transformed to a strip

After the conformal mapping, our problem is now in a strip domain shown in Figure 23.

The boundary condition for $\xi = \dfrac{\pi}{2}$ is $\phi = 1$ and for $\xi = 0$ is $\phi = 0$. The solution in for potential

in the strip in w domain is thus $\phi(\xi, \eta) = \dfrac{2}{\pi} \xi$ and the complex potential at the w domain is thus:

$$F = \phi(\xi, \eta) + i\psi(\xi, \eta) = \frac{2}{\pi}\xi + i\frac{2}{\pi}\eta = \frac{2}{\pi}w. \tag{3.1}$$

The electric field with relation to the complex potential is:

$$-E_x + iE_y = \frac{dF}{dz} = \frac{dF}{dw} \cdot \frac{dw}{dz} = \frac{2}{\pi}\frac{1}{\sqrt{1-z^2}} = \frac{2}{\pi}\frac{1}{\sqrt{1-x^2+y^2-2ixy}}. \tag{3.2}$$

Finally, E_x is expressed as:

$$E_x = -\frac{2}{\pi}[(1-x^2+y^2)^2 + 4x^2y^2]^{-1/4}\sqrt{1+\frac{1-x^2+y^2}{\sqrt{(1-x^2+y^2)^2+4x^2y^2}}}{2}. \tag{3.3}$$

To plot Equation (3.3), we have the analytical E_x along jet surface in Figure 25 (red stars).

3.1.2 Numerical simulation of the electric field

The model of numerical simulation is conducted and the electric potential of butterfly electrodes is shown in Figure 24. To compare the simulation results (black dot in Figure 25) with the analytical model, we simply set both the electric potential and the gap between blade and jet center as 1.
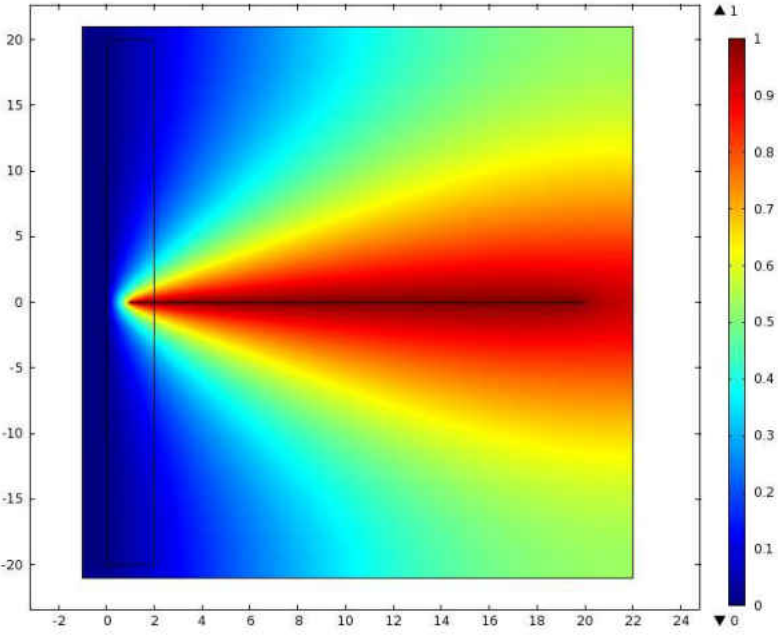
Figure 24: COMSOL simulation for the electric potential of butterfly electrode

The comparison between numerical simulation and analytical solution for Equation (3.3) at location $x=0$ shows decent agreement with each other.
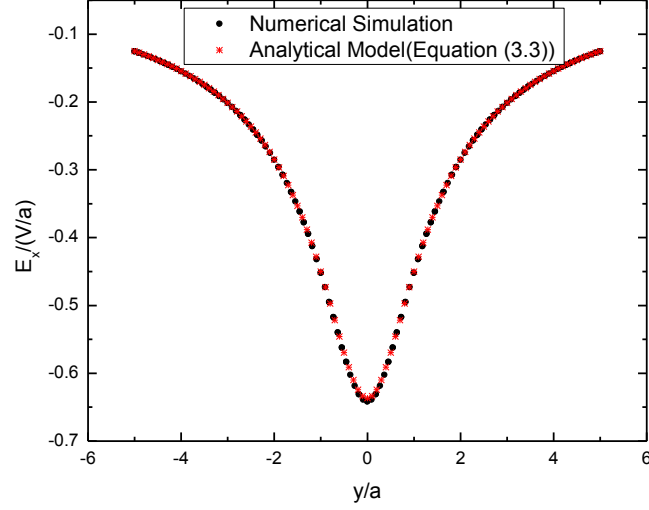
Figure 25: Electric field comparison between Comsol simulation and analytical model

3.2 Perturbation equation of the charged micro-jet

Equation (3.3) is the solution in non-dimensional form, to recover it to dimensional form; the solution is expressed in Equation (3.4):

$$E_x = -\frac{2V}{\pi a}[(1-(\frac{x}{a})^2+(\frac{y}{a})^2)^2+4(\frac{x}{a})^2(\frac{y}{a})^2]^{-1/4}\sqrt{1+\frac{1-(\frac{x}{a})^2+(\frac{y}{a})^2}{\sqrt{(1-(\frac{x}{a})^2+(\frac{y}{a})^2)^2+4(\frac{x}{a})^2(\frac{y}{a})^2}}} \cdot (3.4)$$

Therefore the amplitude of the perturbation can be analyzed using the following simplified model. The fringe electric field for a gap between two thin and flat electrodes is:

$$E = E_0 \cos(\omega t + \phi), \quad E_0 = 2V_{pp} / \pi a[1+(y/a)^2]^{1/2}, \tag{3.5}$$

where V_{pp} is the voltage applied, a is half the distance between two blades and ω is the dimensionless growth rate. The jet surface charge density σ can be calculated from $\sigma=I/v_j$, where I is the current carried by the jet, and v_j is the jet velocity. Consider a small section of the

liquid disk element of the jet $d_m=\rho\pi r^2 dz$, the radial direction acceleration of the element subject to transverse field E is $dv_x/dt=2E\sigma/\rho r_j$. This gives initial perturbation d_s scales with $\underline{E}\sigma/4\rho r_j f^2$, where $\underline{E}$ is the average magnitude of the electric filed as the jet pass the gap. This suggests that the amplitude of the initial jet wave pattern is proportional to f^{-2}, or λ^2. Figure 26 shows the initial perturbation obtained using the above equation and the amplitude measured from high speed images. This simple perturbation amplitude model shows decent agreement with the experiment in section 3.3.
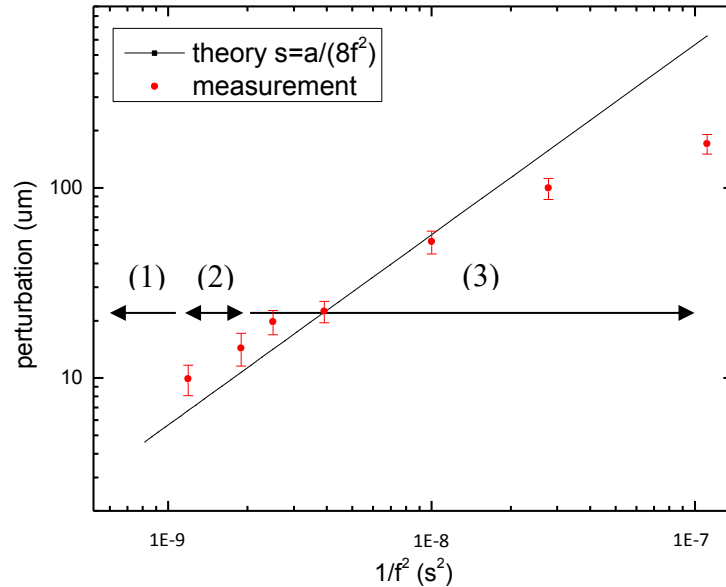
Figure 26: Initial perturbation vs frequency for 8mL/h. (1)short wavelength perturbation (single stream), (2)intermediate perturbation (splitting of jets); and (3)long wavelength perturbation

Next we focus on the short wavelength perturbation region, in which the classic Rayleigh linear theory can be applied. To analyze the perturbation response to the electrical and geometrical parameters of the electrode, we assume the electrified jet is axial symmetric and slender. We further denote jet surface profile as $\xi(z)$, where z is the distance from the blade electrodes, and ξ is the jet radius at location z. The dimensionless growth of perturbation is

31

$$\tilde{\xi} = \Delta\xi / r_0 = \tilde{\xi}_0 \exp(\omega t).$$
(3.6)

Again, following Canan-Calvo (1998), we can write the momentum equation for a slender jet under electric field as:

$$\frac{d}{dz}[P_g + \frac{\gamma}{\xi} - \varepsilon_0 \sigma E + \frac{\rho_l Q^2}{2\pi^2 \xi^4}] = 0,$$
(3.7)

where P_g is the atmosphere pressure, ρ_l is the liquid mass density, and Q is the liquid volumetric flow rate. In Equation (3.7), the combination of the first three terms is the total pressure inside the liquid jet. Further, inexplicit in Equation (3.7) is that both internal viscous loss and the shear stress at the liquid-air interface are neglected.

3.3 Experimental setup and results

3.3.1 Overview of experimental setup

Figure 27 shows the schematic of the experimental setup. The liquids used in this work primarily are 100% ethanol; the mixture of 75 w. % ethanol and 25 w. % glycerol is also used to examine the effect of liquid viscosity. A stable Taylor cone is generated by charging the liquid passing a stainless needle (OD=311μm and ID=159μm) to about 2 kV. The liquid flow rate is from 1 to 8mL/h, corresponding to the jet diameter from about 10μm to 30μm. The typical current carried by the jet is 20 nA. The jet velocity is on the order of 10 m/s. This gives a surface charge density of $3.78 \times 10^{-5} C/m^2$ to $1.07 \times 10^{-4} C/m^2$, which is modest enough to not significantly deviate from the dispersion relationship of neutral jet (Equation (2.7)). The primary effect of the charge on the jet is to provide a means for the jet to be influenced rapidly in the tempo domain as well as localized in the space domain.

(a)
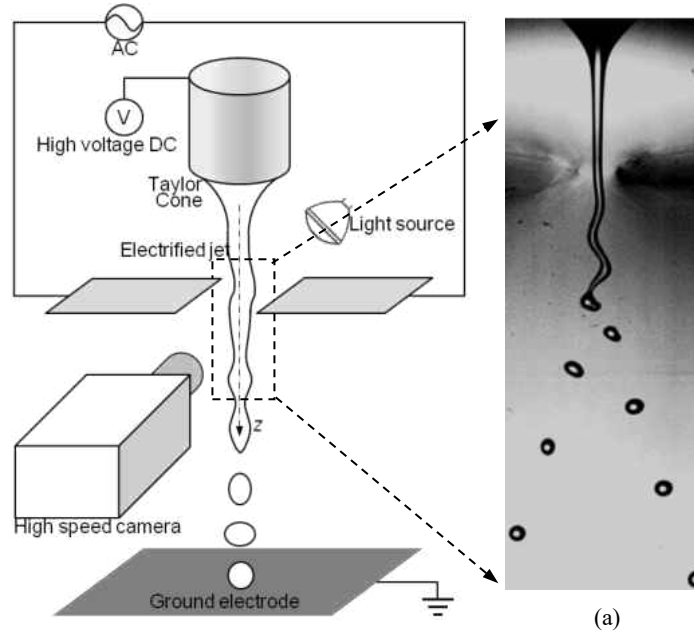
Figure 27: Experimental setup of the jet under transverse electro-hydrodynamic perturbation

The experiment phenomena are recorded with the same high speed camera and LED light in capacitor PEHD chopper experiment. The transverse perturbation is introduced by the fringe electric field in a small gap (<200 μm) between two sharp razor blades on the same plane. Each blade is mounted on an x-y-z linear stage for precise gap adjustment. The two blade electrodes are connected to a sinusoidal alternating current (AC) signal source. The two flat blades essentially form an extractor electrode, allowing intense DC component of the electric field to be established between the nozzle and the blades. At 15 mm below the blade electrodes, an additional electrode at -2 kV is used to guide the charged droplets and avoid the droplet fly-back to blades. The AC signal has adjustable V_{p-p} (peak-to-peak voltage) from 0 to 330V with zero DC offset, and the virtual grand is the same as the DC power supplies. The AC frequency is from 10 kHz to 200 kHz, and the upper limit is imposed by the bandwidth of the AC power supply. The natural oscillation frequency of a liquid meniscus (Taylor cone in this case) can be estimated by

33

$\omega_0 = [\gamma / (\rho R_n^3)]^{1/2}$, where γ is the liquid interfacial tension, ρ is the liquid mass density, and R_n is

the nozzle radius. For a typical nozzle diameter of 300 μm, the Taylor cone oscillation frequency

is below 1 kHz, which is much less than the frequency range of the AC signal applied. Therefore,

despite the fact that the blade electrodes are placed just ~1mm away from the nozzle, the Taylor

cone is not affected by the high frequency AC signal and generates highly stable and

reproducible electrified jets.

3.3.2 Effect of AC signal frequency

Figure 28 shows the response of the liquid jet to the perturbation as AC frequency (and

hence the perturbation wavelength) is varied. The edge of the chopper is perpendicular to the jet

as well as the image plane. The peak driving voltage V_{p-p} and the gap are 300V and 79 μm

respectively. We vary the wavelength of the AC signal, from 3k Hz to 200k Hz. The jet pattern

exhibits the same frequency of the driving signal. At the long wavelength (Figure 28.a), the jet

whips with an amplitude comparable with the wavelength. The amplitude is growing as the jet

travels, because the electrified jet tends to stretch when it is bent. The long wavelength jet breaks

up at all across the jet, without preference near the peaks or valleys of the jet pattern. As the

wavelength reduces (Figure 28.b and 28.c), the jet bending curvature gradually increases,

showing obvious thickened diameter at the peaks/valleys and with thinned jet neck in between.

The jet eventually breaks up at the larger bulbs at the peaks/valleys, with secondary breakup of

the liquid neck into satellites. Under human eyes or regular photography (Figure 28.i), this

breakup appears to be the jet is splitting into two streams.
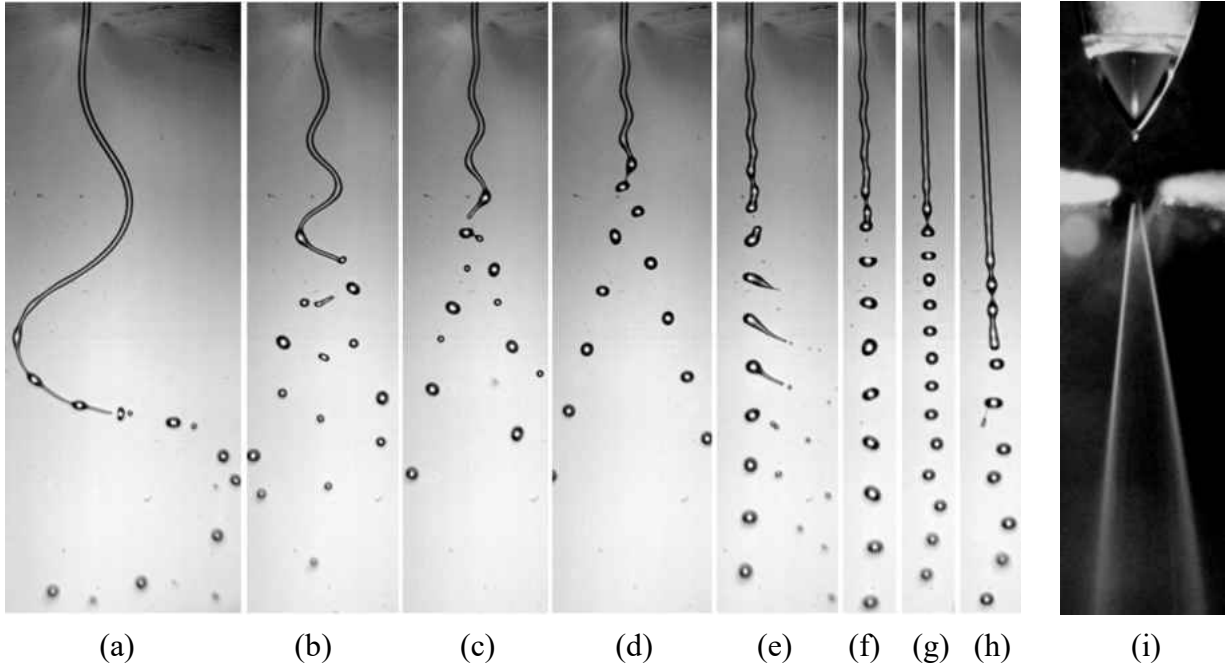
Figure 28: Typical response of the electrified jet to external transverse perturbation introduced by the AC electric field between the narrow gaps of two in-plane blade electrodes. Nozzle inner diameter: 159μm; jet diameter 21μm; gap ~60 μm; shutter speed: 300ns; frame rate: 22000fps

Interestingly, near $2\lambda_R$ (Figure 28.d), the neck between the peaks and valleys becomes essentially zero, resulting very "clean" breakup without any satellite droplets. The jet still appears to split into two streams of droplets. As the wavelength is further reduced, the liquid neck between each pair of peak and valley is not thin enough, and then the peak and valley merge to form a single droplet. However, the surface charge of the droplet exceeds Rayleigh limit of charge, meaning the electric stress overwhelms the surface tension. The Rayleigh limit is expressed as $q = 8\pi\sqrt{\varepsilon_0 \gamma r^3}$, where ε_0 is vacuum permittivity, γ is the surface tension and r is the droplet radius. In the case for pure ethanol, two 10um droplets charged to 70% Rayleigh limit produces a droplet which is charged to 99% Rayleigh limit after merging. In this case, the newly formed droplet immediately experience Coulombic fission (Denis et al, 2003), shedding small daughter droplets to bring the charge level of the main droplet below the Rayleigh limit. Near the

Rayleigh mode, i.e. as the wavelength is close to λ_R, (Figure 28.f and 28.g), the transverse perturbation amplitude is reduced to be small compared to the jet diameter. The small transverse perturbation essentially is converted to longitudinal perturbation, and the jet undergoes typical varicose instabilities. At very short wavelength (Figure 28.h), the perturbation does not destabilize the jet and the jet breaks up similar as natural perturbations instead.

3.3.3 Effect of electrode geometry

Figure 29 (a) and (b) shows the effect of the gap between the two blades on the breakup location (and hence the indirectly on the initial perturbation). The wider gap corresponds to considerably smaller perturbation, and thus longer breakup length (starting from the blade position). Figure 29 (c) has the same gap as that of Figure 29 (b), but the blades are 300 µm closer to the tip of the Taylor cone. The jet breakup is slightly earlier in Figure 29 (c), suggesting a larger initial perturbation.
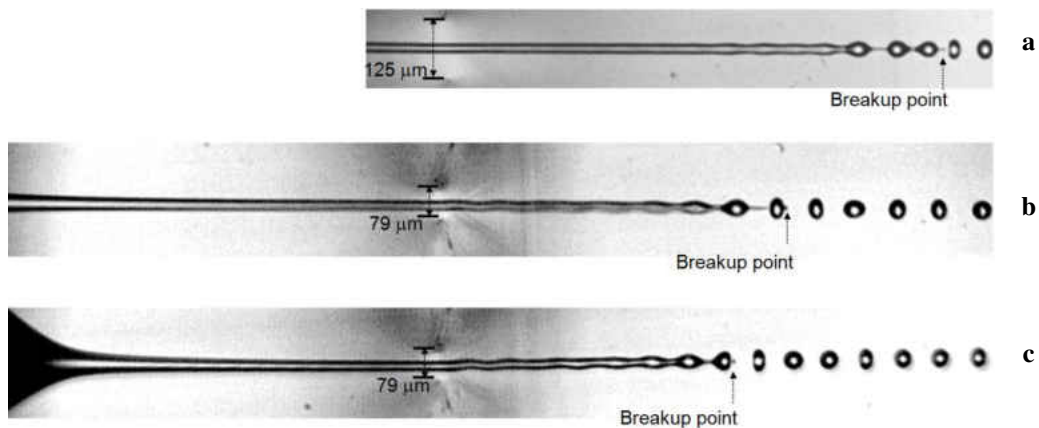
Figure 29: The gap and distance effect on the growth of jet instability. All perturbation frequency is 80kHz, corresponding to a wavelength 125 µm. (a) gap 2a=125 µm; (b) gap 2a=79 µm; (c) same gap with case (b), but the blades are 300 µm closer to the Taylor cone

3.3.4 Governing equation of the perturbation

Since $Q = \pi \xi^2 v_j$, and use $\beta^2 = \rho \xi v_j^2 / \gamma$, we can rewrite Equation (3.5) as:

$$\widetilde{\xi} = \frac{d\xi}{\xi} = -\frac{I \cdot (\partial E / \partial z)}{v_j (2\beta^2 + 1)\gamma / \xi} dz .$$ (3.8)

Equation (3.8) suggests that the perturbation not only scales with the charge density of the jet, but also scales with the gradient along z-direction of the fringe field. In fact, we can still interpret the gradient of the fringe field as an indicator of the "sharpness" of the blade electrodes. Combining Equation (3.5) and (3.8), we obtain:

$$\widetilde{\xi} \propto \frac{\sigma V_{pp} z}{\gamma a^3 [1 + (\frac{z}{a})^2]^{3/2}} .$$ (3.9)

Expression (3.9) suggests that initial perturbation is proportional to V_{pp} and σ but inverse proportional to γ. Reducing blade gap increases $\partial E / \partial z$, leading to a larger initial perturbations.

3.3.5 Perturbation on viscous liquid jet

The viscosity shows strong effects on the jet breakup under transverse perturbation. When pure ethanol is replaced with mixture of 75% ethanol + 25% glycerol, the viscosity is increase by 10 times. Noticeably, the jet is more stable. Compared to pure ethanol jet, the jet of mixture can be stretched longer at long wavelengths before (Figure 30.a). Near twice of the Rayleigh wavelength, thin and long liquid bridges form between two droplets and form the zigzag pattern (Figure 30.b and 30.c).

Detailed understanding of the viscous liquid jet subject to transverse perturbation is beyond the scope of this thesis. However, the experimental results shown here suggest distinct behavior and further investigations are recommended for future research.
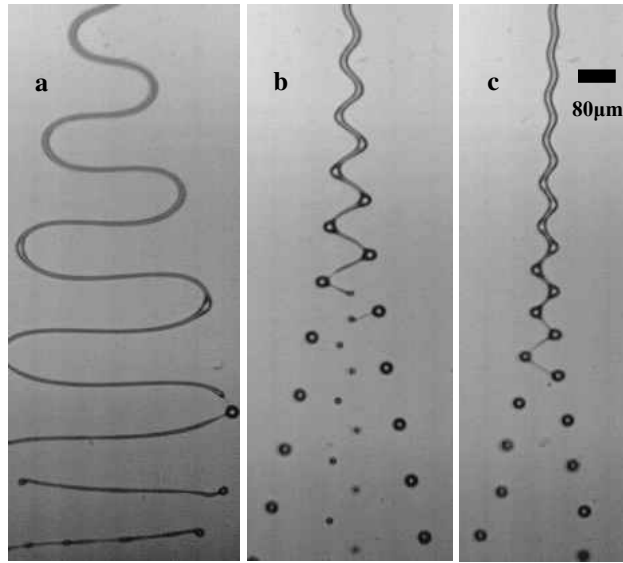
Figure 30: Perturbation response of more viscous liquid (75% ethanol + 25% glycerol)

CHAPTER 4 ELECTROSPRAY PRINTING OF POLYMER DERIVED CERAMICS

4.1 The need for high temperature sensors in harsh environments

Micro-sensors are potentially game-changing devices in many applications, especially in harsh environments such as in gas turbine engines, nuclear reactors, burning buildings, crashed airplanes, and collapsed coal mines. Turbine engines (Figure 31) play a dominant role in power generation and aerospace propulsion. The most critical components in turbine engines are the turbine blades, which are exposed in harsh environments of high temperature (up to 1400 °C), corrosive species (oxygen and water vapor), and high stresses due to centrifugal force at fast rotating speed of around 10,000 rpm. Currently, turbine engine design and lifetime have been limited by the lack of detailed thermo-mechanical information of the turbine blades, especially in hot sections. To provide real time thermal-mechanical measurements for engine control, health monitoring and design optimization, there is a pressing need to establish a manufacturing process that can conformably fabricate embedded sensors on the turbine blade with low profiles that do not disturb the flow field.
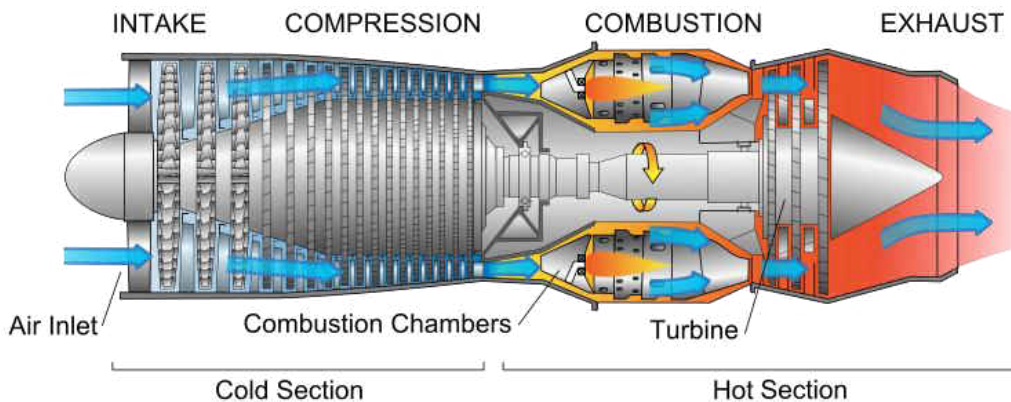
Figure 31: Diagram of a typical large gas turbine engine (Boyce, Meherwan P, 2011)

4.2 Unique property of polymer derived ceramics

Developing sensors embedded on turbine blades is not trivial. The biggest technical challenge is that the sensing materials must survive the extreme environments, including high-temperature and corrosive species both structurally and functionally. Such requirements prevent the use of conventional MEMS materials such as silicon.

One key enabler for sensors in harsh environments is the sensing materials, which must keep the sensing functionality at high temperatures (500-1400°C), elevated pressures (600 psi), high mechanical stress, and corrosive environments. Since 1990s, sensing materials and technology in harsh environments have greatly progressed. The first generation micro-sensors, based on silicon carbide (SiC) and silicon nitride (Si_3N_4) (D. J. Young et al, 2004; P Nieva et al, 1998), can be used in the harsh environments of up to 600°C (An L et al, 2012). Besides the well-defined semiconducting behavior at ultrahigh temperature (Mocaer, D et al, 1993), recently, polymer-derived ceramic (PDC) micro-sensors have attracted extensive attention due to their capability of surviving harsh environments in turbine engines (N R Nagaiah et al, 2006).

PDCs exhibit excellent thermo-mechanical properties at high temperatures. For example, PDCs are thermally stable at temperatures up to 1500°C (Riedel et al, 1996); and their creep resistance exceeds that of polycrystalline SiC and Si_3N_4 (An L et al, 1998). Particularly, aluminum (Al) doped SiCN ceramics (SiAlCN) exhibit an anomalously high resistance to oxidation and hot-corrosion (An L et al, 2004): after being exposed in water vapor and/or NaCl containing environments, typical silicon-based ceramics showed clear signs of corrosion in Figure 32.a, while pyrolyzed PDCs are almost intact.
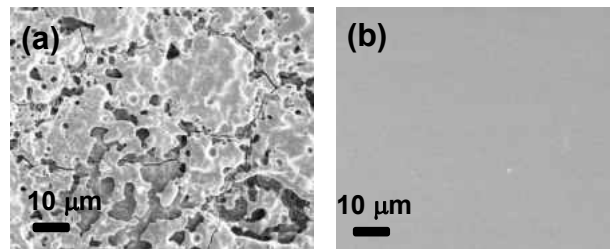
Figure 32: Scanning electron microscope (SEM) images of the surfaces of (a) typical silicon-based ceramics without Al-doping after heat-treatment in water vapor environments, and (b) polymer derived SiAlCN ceramics after annealing at 1400°C for 300 hrs in 50% H_2O-50% O_2 (An L et al, 2004)

Table 1 compares some properties of the SiAlCN with SiC and Si_3N_4. It is clear that besides its excellent oxidation/corrosion resistance, the SiAlCN also possesses much better thermal shock resistance than SiC and Si_3N_4. Therefore, we anticipate that SiAlCN-based sensors are sufficiently corrosion resistant at high temperatures and are suitable in turbine engine environments.

Table 1: Properties of polymer derived SiAlCN and other high-temperature materials (Colombo et al, 2010)

Properties	Polymer derived SiAlCN	SiC	Si_3N_4
Strength (MPa)	**~1000**	~400	~700
Thermal shock FOM*	**1800-3600**	350	880
Oxidation rate (x10^{-18} m^2/s, @1400°C)	**0.47**	16.4	6.2
Corrosion rate (x10^{-6}g/cm^{2}hr, @1400°C, H_2O)	**0.98**	6.4	6.2
Hardness (GPa)	15-20	30	28
Density (g/cm^3)	2.2	3.17	3.19
Fracture toughness (MPa.m$^{1/2}$)	3.5	4-6	5-8
Young's modulus (GPa)	92	400	320
Poisson's ratio	0.18	0.14	0.24
CTE (coefficient of thermal expansion,10^{-6} /K)	3	3.8	2.5

* Thermal shock FOM = strength/(E.CTE)

4.3 Electrospray printing of polymer precursor

PDC microfabrication has been attempted using lithography and micro-molding (L. Liew et al, 2001). These processes require additional mounting step for sensor applications. Hence, to make embedded sensors on the curved surface of the blades of turbine, electrospray is a promising approach to generate monodisperse droplets which will be directly printed on the substrate without mask.

4.3.1 Experiment setup

Figure 33 depicts a typical single ES and the printing setup we used. It consists of three major components: an ES printer head (a 0.4mm diameter stainless steel needle), a heated substrate on an x-y table, and a digital camera coupled with a long working distance microscope. An extractor electrode was added between the ES printer head and the substrate. The extractor is a thin metal plate placed 0.5 mm below the nozzle with a 0.5mm diameter hole to allow the liquid jet to pass through. The extractor typically sits 1 mm above the substrate and serves two functions: first, it isolates the tip of the ES nozzle electrostatically from the rest of the spray, therefore we can adjust the electric field between the extractor and the substrate without disturbing the liquid cone; second, when the substrate is heated to initiate polymer cross-linking, the extractor blocks the heat and to prevent premature cross-linking. The substrate is 2 cm × 2 cm silicon wafer. A PID controlled film heater is placed underneath the substrate, and mounted on the x-y table driven by stepper motors. Each axis of the x-y table moves at an adjustable speed of 0.2-20 mm/s with a resolution of 2 μm. The printing paths or patterns are first designed using CAD software (Solid Works), and then converted into G-code that can be executed by the stepper motor controller.
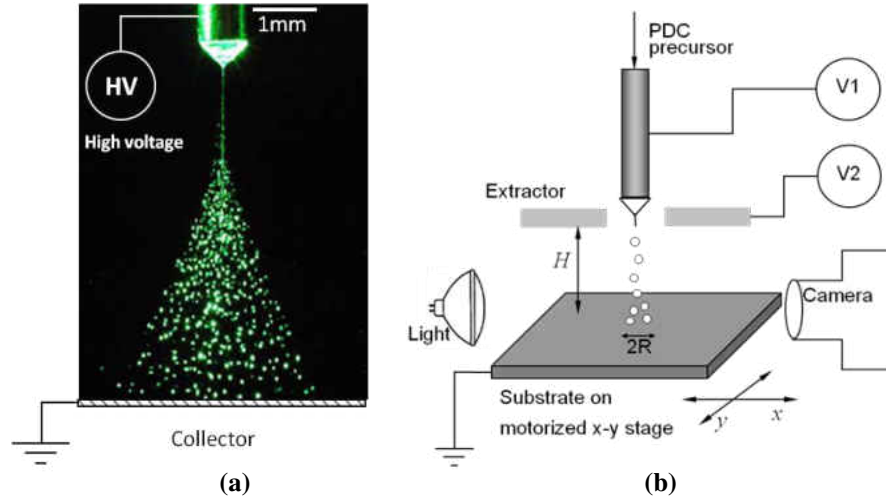
Figure 33: (a) The ES as a printing head, with near-field and far-field schematically illustrated. (b) ES printing setup

The ES nozzle is charged at voltage V_1, while the extractor electrode is charged at V_2. The distance H between the extractor and the substrate is fixed at 1mm. The driving field E, defined as the electric field between the extractor and the substrate, can be adjusted by varying V_2, while keeping V_2-V_1 a constant. The ES is operated in the cone-jet mode, generating quasi-monodispersed droplets with typical relative standard deviation less than 10%. The droplet diameter is tunable from 2 μm to 20 μm by varying the flow rate.

We used two types of ink formula in this work. The first is ethanol with 0.1% volume concentration of 500nm polystyrene latex (PSL) particles. The particles are dyed into blue color by the manufacturer. Ethanol is a liquid with good electrospraying properties. The electrical conductivity K of the ethanol ink is measured at $K=6.3\times10^{-4}$ S/m. This ink formula is relatively less hazardous and it allows us to systematically investigate the printed line-width.

The second ink formula uses acetone as solvent to dissolve the PDC precursor. The PDC precursor used in this study is HTT1800 Ceraset (KiON Group), which is a liquid polysilazane-based precursor for SiCN ceramics. The ink formula was varied from 4 to 50% (by volume) PDC

precursor dissolved in acetone. After printing, the acetone evaporates leaving only PDC on the substrate. After subsequent pyrolysis at 1000°C in nitrogen, the precursor is converted to SiCN ceramics.

4.3.2 Printed line-width as a function of driving fields

We have derived a spray profile model to describe how R (the radius of the electrospray) expands (W. Yang et al, 2012):

$$R = (x_R x)^{1/2} \text{ , where } x_R = I_0 / (\varepsilon_0 \pi E_d^2 Z) , \tag{4.1}$$

where I_0 is the current carried by the spray, ε_0 is the air permittivity, E_d is the driving field, and Z is the mobility of the charged droplet. Equation (4.1) suggests the ES profile is parabolic if viewed from the direction perpendicular to the spray axis. Moreover, the spray diameter is inversely proportional to the intensity of the driving field.

We also numerically studied the spray profile with the Lagrangian method (A.M. Ganan-Calvo et al, 1994; Wilhelm et al 2003; Deng et al, 2007; Oh et al, 2008), which tracks each droplet in a dilute two-phase flow by considering the force acted on each individual droplet. Figure 34 shows the comparison of the results from experiment, analytical model (Equation (4.1)) and the Lagrangian model.
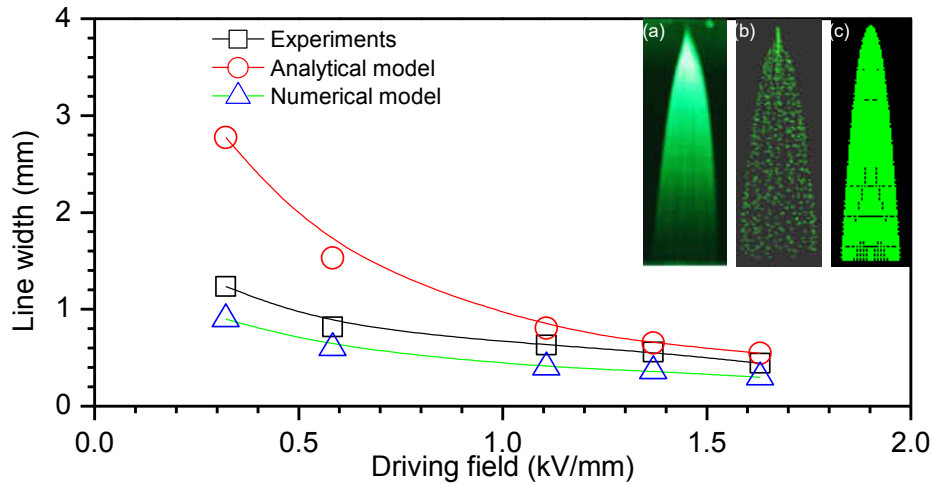
Figure 34: Effect of driving field on line-width. The inset is the typical ES profile images from (a) experiments, (b) numerical simulation using Lagrangian model, and (c) spray profile model.

We noticed that the results from analytical model and the numerical model bracket the experimental data. Specifically, the analytical model consistently over-predicted the line-width, especially at low driving field range. (Figure 34) This discrepancy is because we assumed the droplet has no inertia in deriving (1). However, in near-field ES, the droplets still have significant momentum after jet break-up. This makes the inertia-less assumption break down and introduce noticeable errors. Nevertheless, the simple analytical model is valuable in predicting an upper limit of the line-width. On the other hand, the measured line-width is consistently wider than the numerical model, because the deposited polymer droplets may merge together and overflow to sideways before it is completely solidified or cross-linked. The difference between the measured results and the numerically predicted value is almost a constant of 200 μm. One possible explanation for this phenomenon is that in the numerical code, we prescribed strictly monodisperse droplet; however, in a real electrospray, a typical relative standard deviation of 10% is expected. Smaller droplets tends to be affected by the space charge field along the radial direction more, therefore the real spray appears to be wider than the numerically simulated one.

45

4.3.3 Pyrolysis of printed PDC

The pyrolysis process was carried out in a tube furnace, during which the samples were protected by continuous nitrogen and heated up to 1000 °C. The typical pyrolysis procedure is shown in Figure 35. The rate of temperature rise changed from 1°C/min to 0.5°C/min. This rate change helps protect the integrity of the samples during shrinkage. The designed constant temperature at 200 °C, 400 °C and 1000 °C is to ensure that the samples have enough time for shaping, cross-linking and pyrolysis. Especially, to handle thicker deposition (≥10μm), the rate of temperature rise needs to be further decreased.
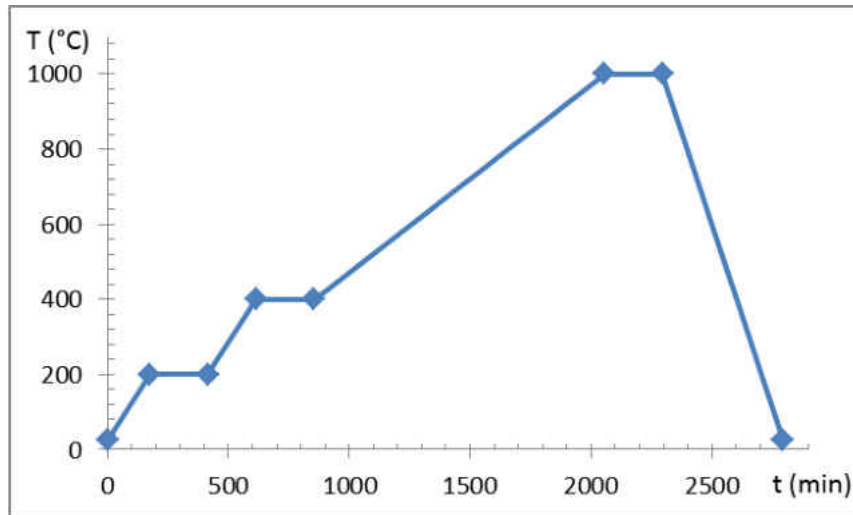

Figure 35: Pyrolysis process which undergoes in nitrogen environment

We first examined the pyrolysis of a simple straight line printed by near-field ES. We achieved the line width as narrow as 35μm in Figure 36. The thickness can be varied by adjusting the printing speed and/or the number of the printing paths repeated. The printed line kept integrity after pyrolysis.
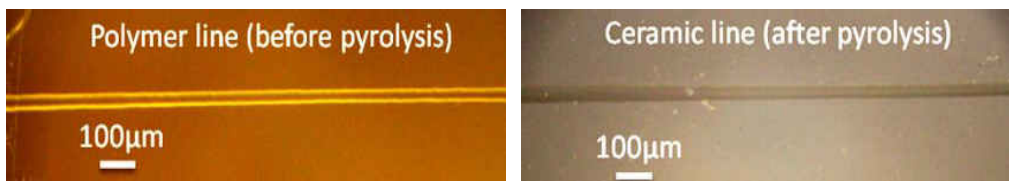
Figure 36: 1D PDC feature from ES printing

The thickness of the line printed after a single path is on the order of 100 nm for 4% PDC precursor concentration, 0.2 mL/h ink flow rate, and 1 kV/mm driving fields. Multiple paths, higher PDC concentration, and/or stronger driving field can lead to trace thicker than 10μm.

Next, to show the capability of printing micro patterns, we used the near-field printing setup (Figure 33) to create a micro pentagram pattern from the precursor. After pyrolysis, the entire pattern was kept intact, and the edges and apexes of the pentagram remained well-defined. The printed pattern firmly adhered to the silicon substrate, and it could not be removed by scratching with a sharp razor blade. Moreover, the ceramic pattern shows very high surface quality which is crucial in sensor fabrication. We found no obvious cracks under 5300x magnification under SEM across the entire 2 mm wide pentagram. Meanwhile, the printed pattern appeared to be smooth, uniform, and continuous.
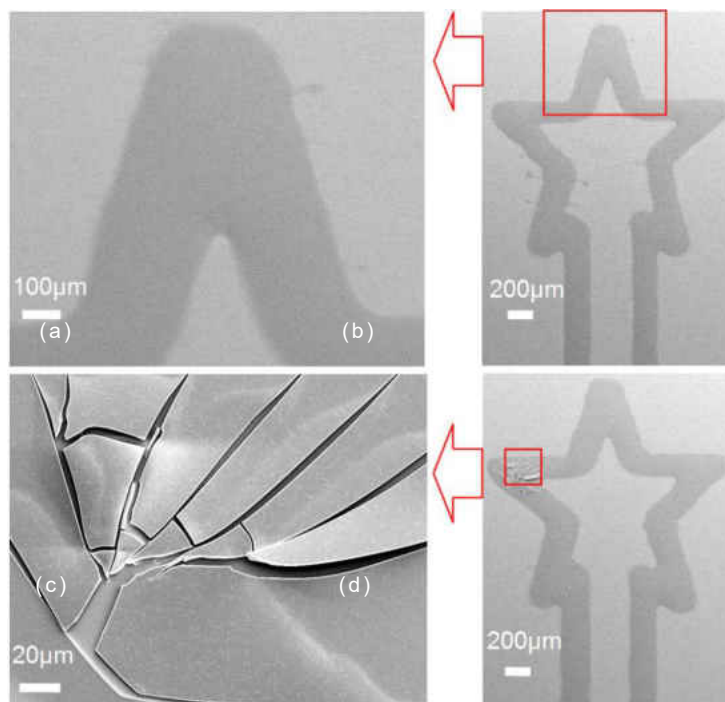
Figure 37: SEM images of (a)(b) A good sample of micro pentagram produced by near-field ES printing and (c)(d) A cracked sample.

We note, however, that certain experiment conditions can lead to cracked samples, such as the one shown in Figure 37. Our experience suggests the following practices are critical for preventing cracks: (1) Clean substrate thoroughly, especially make sure the substrate is free of dust (or solid particle), because during the pyrolysis, dust particle under the polymer layer may add on to the asymmetrical stress; (2) Sonicate the ink/precursor vigorously to remove micro bubbles in the solution; and (3) Choose an appropriate substrate temperature. In this study, 70-80 °C gave best results, because on one hand this temperature is close to the boiling point of acetone to rapidly evaporate the solvent and prevent spread of the printed pattern, while on the other hand the temperature is modest enough to avoid active release of gas such as ammonia during the cross-link.

4.3.4 Analysis of the deposition shrinkage

After pyrolysis, the materials shrink due to mass loss from thermal decomposition. To study the shrinkage of the polymer after pyrolysis, we first dissected a 1-D sample (perpendicular to the line direction) to create two identical cross-sections. One of the dissected samples went through normal pyrolysis. Then we measured cross-section profiles for the simply cross-linked polymer sample and the pyrolyzed sample using a profiler (Tencor Alpha 200). The results in Figure 38 reveal the shrinkage along the width and thickness directions are 9% and 38% respectively. The discrepancy in two directions is caused by the constriction of the substrate adhesion. We further estimate the bulk shrinkage is approximately 49%.
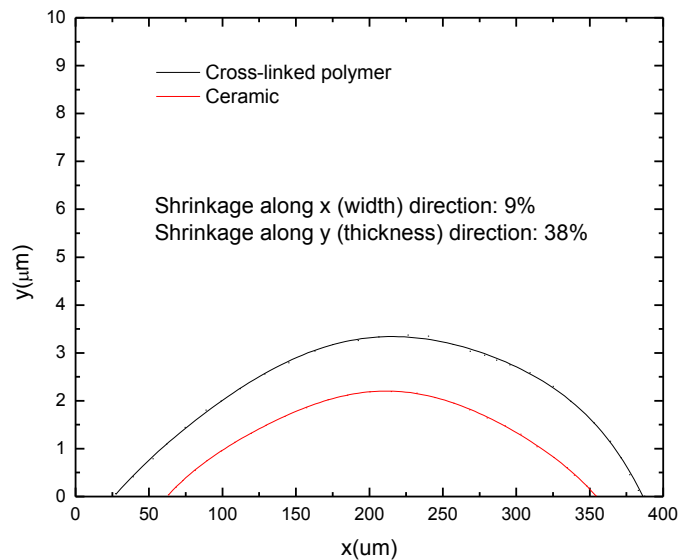

Figure 38: Surface profile measurement of the samples

CHAPTER 5 CONCLUSION

This thesis studied a non-intrusive approach to induce transverse periodic perturbations on micro liquid jets to generate strictly monodisperse droplets. The operating principle is to exploit the fringe field of a thin capacitor that is driven by sinusoidal signals to induce periodic electro-hydrodynamic stress and "chop" the liquid jet. The instability grows fastest when the driving signal is near 50% of the Rayleigh frequency. The initial induced perturbation is proportional to the driving voltage squared. The liquid jets experience highly ordered break-up whose size relative standard deviation is less than 0.01. We demonstrate that the approach is scalable through showing chopping effect on multiple jets.

Furthermore, we combined a modified butterfly PEHD chopper with a typical electrospray. We show the finer jet produced by ES subject to the PEHD chopper and can generate highly monodisperse droplets with diameter smaller than 50μm. We also studied the jet breakup behaviors with varied AC frequency and amplitude. Due to the sensitive response to the AC signal, the jet and droplets manipulated by butterfly PEHD chopper can probably be utilized for electro-spinning and Nano fabrication respectively. For further study and its potential, PEHD chopper can be easily scaled up and combined with other droplet generation such as flow focusing.

Finally we showed a novel method to directly print micro patterns of polymer derived ceramics (PDC) near-field electrospray. The PDC precursor liquids can be printed reliably without any clogging issues. The self-expansion due to Coulombic repulsion amongst charged

droplets can be suppressed by decreasing the droplet residence time through reduced distance between the substrate to the extractor, or increased driving fields. The spray expansion model can estimate the line-width and the prediction is in decent agreement with the experimental results at relatively high driving fields (>1 kV/mm). We have demonstrated PDC 1D features as narrow as 35 μm, as well as a 2D pattern of a micro pentagram. Moreover, after pyrolysis at 1000 °C in nitrogen, the amorphous alloys of silicon, carbon and nitrogen (SiCN) was formed. The ceramic layer firmly adhered to the substrate without cracks. The material shrinkage along width and thickness directions is measured at 9% and 38% respectively. Our study shows that this maskless, scalable, bottom-up fabrication technique is a useful addition to the tool box for ceramic MEMS. The relative topic for further study will be to use ES achieving PDC 3D printing. To this end, we recommend that a tapered nozzle with inner diameter smaller than 50μm is necessary for better and stable control of ES. More importantly, processing cross-linked or higher than 50% (volume) PDC precursor, as well as pyrolysis procedure will be crucial for the surface quality of PDC.

REFERENCES

An, L., Riedel, R., Konetschny, C., Kleebe, H., & Raj, R. (1998). Newtonian viscosity of amorphous silicon carbonitride at high temperature. Journal of the American Ceramic Society, 81(5), 1349-1352.

An, L., Wang, Y., Bharadwaj, L., Zhang, L., Fan, Y., Jiang, D., ... & Chow, L. C. (2004). Silicoaluminum carbonitride with anomalously high resistance to oxidation and hot corrosion. Advanced Engineering Materials, 6(5), 337-340.

Berglund, R. N., & Liu, B. Y. (1973). Generation of monodisperse aerosol standards. Environmental Science & Technology, 7(2), 147-153.

Boyce, M. P. (2011). Gas turbine engineering handbook. Butterworth-Heinemann.

Crowley, J. M. (1983). Electrohydrodynamic droplet generators. Journal of Electrostatics, 14(2), 121-134.

Chandrasekhar, S. (1981). Hydrodynamic and hydromagnetic stability. Dover publications.

Colombo, P., Mera, G., Riedel, R., & Sorarù, G. D. (2010). Polymer-Derived Ceramics: 40 Years of Research and Innovation in Advanced Ceramics. Journal of the American Ceramic Society, 93(7), 1805-1837.

Deng, W., Klemic, J. F., Li, X., Reed, M., & Gomez, A. (2007). Liquid fuel combustor miniaturization via microfabrication. Proceedings of the Combustion Institute, 31, 2239-2246.

Deng, W., Waits, C. M., Morgan, B., & Gomez, A. (2009). Compact multiplexing of monodisperse electrosprays. Journal of Aerosol Science,40(10), 907-918.

Duft, D., Achtzehn, T., Müller, R., Huber, B. A., & Leisner, T. (2003). Coulomb fission: Rayleigh jets from levitated microdroplets. Nature, 421, 128.

Donnelly, R. J., Glaberson, W., Donnelly, R. J., & Glaberson, W. (1966). Experiments on the capillary instability of a liquid jet. Proceedings of the Royal Society of London. Series A. Mathematical and Physical Sciences, 290(1423), 547-556.

Eggers, J., & Villermaux, E. (2008). Physics of liquid jets. Reports on progress in physics, 71(3), 036601.

Eggers, J. (1997). Nonlinear dynamics and breakup of free-surface flows.Reviews of modern physics, 69(3), 865.

González, H., & García, F. J. (2009). The measurement of growth rates in capillary jets. Journal of Fluid Mechanics, 619(1), 179-212.

Goedde, E. F., & Yuen, M. C. (1970). Experiments on liquid jet instability. J. Fluid Mech, 40(3), 495-511.

Ganan-Calvo, A. M., Lasheras, J. C., Davila, J., & Barrero, A. (1994). The electrostatic spray emitted from an electrified conical meniscus. Journal of aerosol science, 25(6), 1121-1142.

Gañán-Calvo, A. M. (1998). Generation of steady liquid microthreads and micron-sized monodisperse sprays in gas streams. Physical review letters,80(2), 285-288.

Gong, X., An, L., & Xu, C. (2012, March). Wireless passive sensor development for harsh environment applications. In Antenna Technology (iWAT), 2012 IEEE International Workshop on (pp. 140-143). IEEE.

Hrdina, D. W., & Crowley, J. M. (1989). Drop-on-demand operation of continuous jets using EHD techniques. Industry Applications, IEEE Transactions on, 25(4), 705-710.

Lin, S. P., & Reitz, R. D. (1998). Drop and spray formation from a liquid jet.Annual Review of Fluid Mechanics, 30(1), 85-105.

Liew, L. A., Zhang, W., Bright, V. M., An, L., Dunn, M. L., & Raj, R. (2001). Fabrication of SiCN ceramic MEMS using injectable polymer-precursor technique. Sensors and Actuators A: Physical, 89(1), 64-70.

Liew, L. A., Liu, Y., Luo, R., Cross, T., An, L., Bright, V. M., ... & Raj, R. (2002). Fabrication of SiCN MEMS by photopolymerization of pre-ceramic polymer. Sensors and Actuators A: Physical, 95(2), 120-134.

Lojewski, B., Yang, W., Duan, H., Xu, C., & Deng, W. (2013). Design, Fabrication, and Characterization of Linear Multiplexed Electrospray Atomizers Micro-Machined from Metal and Polymers. Aerosol Science and Technology,47(2), 146-152.

Mocaer, D., Pailler, R., Naslain, R., Richard, C., Pillot, J. P., Dunogues, J., ... & Taulelle, F. (1993). Si-CN ceramics with a high microstructural stability elaborated from the pyrolysis of new polycarbosilazane precursors. Journal of materials science, 28(10), 2615-2631.

Melcher, J. R., & Taylor, G. I. (1969). Electrohydrodynamics: a review of the role of interfacial shear stresses. Annual Review of Fluid Mechanics, 1(1), 111-146.

Nagaiah, N. R., Kapat, J. S., An, L., & Chow, L. (2006, April). Novel polymer derived ceramic-high temperature heat flux sensor for gas turbine environment. In Journal of Physics: Conference Series (Vol. 34, No. 1, p. 458). IOP Publishing.

Nieva, P., Tada, H., Zavracky, P., Adams, G., Miaoulis, I., & Wong, P. (1998, January). Mechanical and thermophysical properties of silicon nitride thin films at high temperatures using in-situ MEMS temperature sensors. In MRS Proceedings (Vol. 546, No. 1). Cambridge University Press.

Oh, H., Kim, K., & Kim, S. (2008). Characterization of deposition patterns produced by twin-nozzle electrospray. Journal of Aerosol Science, 39(9), 801-813.

Parker, G. W. (2002). Electric field outside a parallel plate capacitor. American Journal of Physics, 70, 502.

Qian, S. X., Snow, J. B., Tzeng, H. M., & Chang, R. K. (1986). Lasing droplets: highlighting the liquid-air interface by laser emission. Science (New York, NY),231(4737), 486.

Rezanka, I., & Crowley, J. M. (1990). Satellite control by direct harmonic excitation. Journal of imaging technology, 16(1), 43-47.

Rayleigh, L. (1879). On the stability, or instability, of certain fluid motions.Proceedings of the London Mathematical Society, 1(1), 57-72.

Riedel, R., Ruwisch, L. M., An, L., & Raj, R. (1998). Amorphous silicoboron carbonitride ceramics with anomalously high resistance to creep. J. Am. Ceram. Soc, 81, 3341-4.

Riedel, R., Kienzle, A., Dressler, W., Ruwisch, L., Bill, J., & Aldinger, F. (1996). A Silicoboron Carbonitride Ceramic Stable to 2000° C. ChemInform,27(51), 796-798.

Riedel, R., Ruswisch, L. M., An, L., & Raj, R. (2005). Amorphous silicoboron carbonitride ceramic with very high viscosity at temperatures above 1500 C.Journal of the American Ceramic Society, 81(12), 3341-3344.

Rutland, D. F., & Jameson, G. J. (1971). A non-linear effect in the capillary instability of liquid jets. J. Fluid Mech, 46(2), 267-271.

Taylor, G., & Taylor, G. (1964). Disintegration of water drops in an electric field.Proceedings of the Royal Society of London. Series A. Mathematical and Physical Sciences, 280(1382), 383-397.

Vukasinovic, B., Smith, M. K., & Glezer, A. (2007). Dynamics of a sessile drop in forced vibration. Journal of Fluid Mechanics, 587, 395.

Wilhelm, O., Mädler, L., & Pratsinis, S. E. (2003). Electrospray evaporation and deposition. Journal of aerosol science, 34(7), 815-836.

Yang, W., Lojewski, B., Wei, Y., & Deng, W. (2011). Interactions and deposition patterns of multiplexed electrosprays. Journal of Aerosol Science.

Young, D. J., Du, J., Zorman, C. A., & Ko, W. H. (2004). High-temperature single-crystal 3C-SiC capacitive pressure sensor. Sensors Journal, IEEE, 4(4), 464-470.

Zill, D. G., & Wright, W. S. (2009). Advanced engineering mathematics. Jones & Bartlett Learning.